Article

Classification of Ultrafine Particles Using a Novel 3D-Printed Hydrocyclone with an Arc Inlet: Experiment and CFD Modeling

Yanxia Xu,* Junxiang Ye, Xingfu Song, and Jianguo Yu

Cite This: *ACS Omega* 2023, 8, 998−1016

Read Online

ACCESS | Metrics & More | Article Recommendations

ABSTRACT: Ultrafine particle classification can be realized using hydrocyclones with novel structures to overcome the limitations of conventional hydrocyclones with tangential inlets or cone structures. Herein, the hydrocyclones with different inlet structures and cone angles were investigated for classifying ultrafine particles. Computational fluid dynamics (CFD) simulations were performed using the Eulerian−Eulerian method, and ultrafine MnO_2 powder was used as a case study. The simulation results show a fine particle (≤ 5 μm) removal efficiency of 0.89 and coarse particle (>5 μm) recovery efficiency of 0.99 for a hydrocyclone design combining an arc inlet and a 30° cone angle under a solid concentration of 2.5 wt %. Dynamic analysis indicated that the novel arc inlet provided a preclassification effect to reduce the misplacement of fine/coarse

particles, which cannot be provided by conventional tangential or involute inlets. Furthermore, the proposed design afforded comprehensive improvement in the flow field by regulating the residence time and radial acceleration. Subsequently, a novel hydrocyclone with an arc inlet and 30° cone angle was manufactured using the three-dimensional (3D) printing technology. Experiments were conducted for classifying ultrafine MnO_2 particles using the novel 3D-printed hydrocyclone and conventional hydrocyclone. The results demonstrate that the classification performance of the 3D-printed hydrocyclone was superior to that of the conventional one, in particular, the removal efficiency of fine particles from 0.719 to 0.930 using a 10 wt % feed slurry.
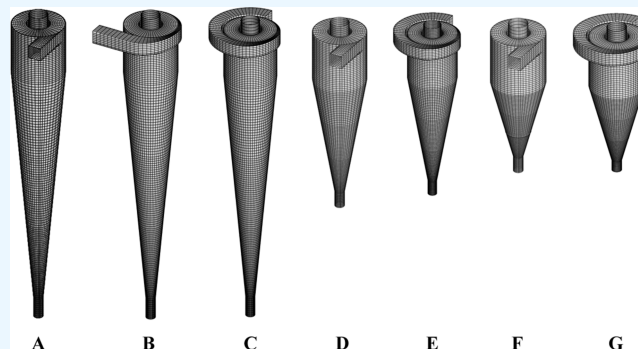
1. INTRODUCTION

Particle ultrafineness is crucial for powder products to achieve optimal performance, particularly in the fields of pharmaceuticals, chemical engineering, electronics, and materials. Several techniques to classify powder particles have been reported, such as microfiltration membranes,[1] flotation,[2] centrifugation,[3] and cyclones.[4] Hydrocyclones are considered a promising alternative for classifying ultrafine particles[5−10] owing to their numerous advantages, such as high efficiency, low energy consumption and commercial cost, large capacity, and compactness. However, the main limitation of hydrocyclones with respect to micron-scale particles is their imprecise classification due to the misplacement of fine and coarse particles caused by stochastic fluctuations, entrainment, short-circuit flows, etc.[11−13] It is well known that the performance of a hydrocyclone is largely determined by its geometrical structure.[14−18] Therefore, increasing attention has been paid to novel structural designs to overcome the separation limitations of the conventional hydrocyclone structure.[19−25]

The diameter of the hydrocyclone body can be determined using several design models,[26,27] whereas other details require more careful investigation. For example, Ji et al.[28] developed a numerical correlation formula to predict the separation performance of hydrocyclones with different geometric

structures. Hsu and Wu[29] recommended an appropriate vortex finder depth to improve separation performance. Ghodrat et al.[30] evaluated the optimal spigot diameter and body size for feeds with various solid concentrations (SCs) and concluded that the diameter and shape of the vortex finder had a greater impact on particle separation than its depth.[31] Wang et al.[32] used a novel membrane tube as the vortex finder of a hydrocyclone to reduce the overflow exit and short-circuit flow, which improved separation performance. Yamamoto et al.[33] investigated several spigot designs and achieved the highest separation performance with an inclined ring, center rod, and apex cone. Lanyue et al.[34] experimentally studied the separation performance of a hydrocyclone with a compound curve cone.

Because the inlet introduces the feed slurry into the main body of the hydrocyclone, its design is important for optimal
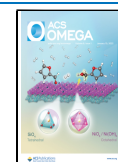
separation performance.[35,36] To improve the separation efficiency, some recommendations for the size and number of inlets were summarized by Hwang et al.[37] A multi-inlet design was also applied in a three-dimensional (3D)-printed mini-hydrocyclone developed by Shakeel Syed et al.[38] to separate microalgae. Fan et al.[39] investigated the optimal inlet section angle using the particle imaging velocimetry (PIV) technique and obtained a considerably improved separation efficiency compared to the conventional design. A novel tangent-circle inlet design reported by Zhang et al.[40] showed better separation performance for ultrafine micron-scale particles than the conventional tangential inlet hydrocyclone. Fu et al.[41] developed a novel inlet particle-sorting cyclone that exhibited good performance for the separation of $PM_{2.5}$. A similar inlet design was applied to submicron-scale particle separation in a mini-hydrocyclone, which improved the separation efficiency considerably.[42]

The conical section is another important component that considerably influences the performance of a hydrocyclone, especially in the case of a small hydrocyclone. A high separation efficiency was achieved for fine particles using a longer conical section in the studies of Wang and Yu[43] and Qi et al.[44] Yoshida et al.[45] observed a decrease in particle cut size with increasing conical length of an electrical hydrocyclone. A similar effect was observed in liquid−liquid separation experiments conducted by Qian et al.[46] However, Wang et al.[47] reported that in a large hydrocyclone, this effect was negligible for coarse (mm sized) particles. Furthermore, several novel cone designs have been presented, including a combined cone hydrocyclone designed with a large upper cone angle by Yang et al.[48] They found that this design led to more micron-scale particles in the underflow, and a smaller angle disparity between the two cones afforded higher separation sharpness. Dong et al.[49] reported a cyclone column separator with complicated positive and negative cones that provided better classification performance than a single cone hydrocyclone. Subsequently, Ghodrat et al.[50] investigated a series of cone section shapes and determined the optimum cone length and shape parameters. Recently, Vega-Garcia et al.[51] developed a novel 3D-printed 10 mm hydrocyclone with a concave parabolic conical wall; experiments and computational fluid dynamics (CFD) simulations demonstrated improved solid recovery with this design. Further, 3D printing helped overcome the design limitations of novel or mini-hydrocyclones in manufacturing.

As mentioned, a novel structural design is key to the development of high-sharpness classification. Furthermore, deeper understanding of the fluid field in a hydrocyclone is necessary to direct its design. Herein, electrolytic manganese dioxide (MnO_2) has been investigated as a case study owing to the manufacturers' requirement for classification. To improve the MnO_2 classification performance of hydrocyclones, the inlet structure and cone angle were altered under different feed SCs and the performance studied using CFD simulations. Furthermore, detailed dynamic analysis demonstrates the mechanism of simulation separation performance. These results provide important details for the design of novel high-sharpness hydrocyclones. 3D printing was adopted for the construction of a novel hydrocyclone owing to its advantages of rapid manufacturing and high resolution, and the hydrocyclone was subjected to separation experiments to verify its effect. Thus, an optimization flow sheet of novel hydrocyclone

classification has been developed via CFD simulation analysis and rapid 3D printing.

2. MATERIALS AND METHODS

2.1. CFD Simulation Methods. *2.1.1. Simulation Model.* The flow fields within a hydrocyclone can be treated as the superposition of three levels: turbulence, water−air core multiphase flow, and multiphase flow with particles. Thus, various CFD models were adopted to describe different levels of flow phenomena. As shown in eqs 1 and 2, the Reynolds stress model (RSM) was used as the turbulence model in this study, as its reliability in the CFD simulations of hydrocyclones has been confirmed in previous studies.[52−54]

$$\frac{\partial}{\partial t}(\rho u_i) + \frac{\partial}{\partial x_j}(\rho u_i u_j)$$
$$= -\frac{\partial p}{\partial x_i} + \frac{\partial}{\partial x_j}\left[\mu\left(\frac{\partial u_i}{\partial x_j} + \frac{\partial u_j}{\partial x_i}\right)\right] + \frac{\partial}{\partial x_j}(-\rho\overline{u_i'u_j'}) \tag{1}$$

where u, ρ, and μ are the liquid velocity, density, and viscosity, respectively. The Reynolds stress term $-\rho\overline{u_i'u_j'}$ is modeled by eq 2.

$$\frac{\partial}{\partial t}(\rho\overline{u_i'u_j'}) + \frac{\partial}{\partial x_k}(\rho u_k\overline{u_i'u_j'}) = D_{T,ij} + P_{ij} + \phi_{ij} + \varepsilon_{ij} \tag{2}$$

where $D_{T,ij}$ is the turbulent diffusion, P_{ij} is the stress production term, ϕ_{ij} is the pressure strain term, and ε_{ij} is the dissipation term.

The volume of fluid (VOF) model was used to capture the water−air phase interface. The tracking of the interface of the air core in hydrocyclones was achieved by solving a single set of momentum equations as follows

$$\frac{\partial\alpha_k}{\partial t} + \frac{\partial(u_i\alpha_k)}{\partial x_i} + \frac{\partial(u_j\alpha_k)}{\partial x_j} = 0 \tag{3}$$

where α_k is the volume fraction of the kth phase.

A single momentum equation was solved throughout the computational domain; then, the resulting velocity field was shared between the phases. For a k phase, the volume-fraction−average density ρ and viscosity μ are determined as follows

$$\rho = \sum_{k=1}^{2}\alpha_k\rho_k \tag{4}$$

$$\mu = \sum_{k=1}^{2}\alpha_k\mu_k \tag{5}$$

All of the other properties were computed in the same manner. After the basic liquid−air flow field in the hydrocyclone has been established, the VOF model was replaced by the two-fluid model (TFM), and the particle phases were introduced into the calculation domain with the application of the kinetic theory of granular flow (KTGF) under an Eulerian frame. Since there were about 10−15 particle phases with different particle sizes needing to be set in this hydrocyclone simulation to ensure the authenticity of the simulated particle system, the mixture model, as a simplified two-fluid model, was selected in this work to balance the computational cost and the simulation accuracy. The mixture model adopts the mixture continuity

equation and momentum equations that are shared by all phases

$$\frac{\partial \rho_m}{\partial t} + \frac{\partial \rho_m u_m}{\partial x_i} = 0 \tag{6}$$

$$\frac{\partial \rho_{\mathrm{m}} u_{\mathrm{m}i}}{\partial t} + \frac{\partial \rho_{\mathrm{m}} u_{\mathrm{m}i} u_{\mathrm{m}j}}{\partial x_i}$$

$$= -\frac{\partial p}{\partial x_i} + \frac{\partial}{\partial x_i}\left(\sum_{k=3}^{n} p_k\right) + \frac{\partial}{\partial x_j}\left[\mu_m\left(\frac{\partial u_{\mathrm{m}i}}{\partial x_j} + \frac{\partial u_{\mathrm{m}j}}{\partial x_i}\right)\right]$$

$$+ \frac{\partial}{\partial x_j}(-\rho_{\mathrm{m}}\overline{u'_{\mathrm{m}i}u'_{\mathrm{m}j}}) + \frac{\partial}{\partial x_j}\left(\sum_{k=1}^{n}\rho_k u_{\mathrm{dr},ki}u_{\mathrm{dr},kj}\right) + g\rho_{\mathrm{m}} \tag{7}$$

where g is the gravitational acceleration, u_{dr} is the drift velocity, and $-\rho_m\overline{u'_{\mathrm{m}i}u'_{\mathrm{m}j}}$ is the Reynold stress term. The density of the mixture, ρ_{m}, the mass-averaged velocity, $u_{\mathrm{m}i}$, and the mixture viscosity, μ_{m}, are defined as follows

$$\rho_{\mathrm{m}} = \sum_{k=1}^{n} \alpha_k \rho_k \tag{8}$$

$$u_{\mathrm{m}i} = \frac{\sum_{k=1}^{n} \alpha_k \rho_k u_{ki}}{\rho_{\mathrm{m}}} \tag{9}$$

$$\mu_{\mathrm{m}} = \sum_{k=1}^{n} \alpha_k \mu_k \tag{10}$$

where α_k, as the volume fraction of the kth phase, is obtained from the continuity equation of phase k.

The drift velocity $u_{\mathrm{dr},ki}$ is achieved from the algebraic model

$$u_{\mathrm{dr},ki} = \frac{(\rho_k - \rho_{\mathrm{m}})d_k^2}{18\mu_1 f_{\mathrm{drag}}}a_{k,i} - \frac{\eta_t}{\sigma_t}\left(\frac{\nabla\alpha_k}{\alpha_k} - \frac{\nabla\alpha_1}{\alpha_1}\right)$$

$$- \sum_{k=1}^{n}\frac{\alpha_k \rho_k u_{1k,i}}{\rho_{\mathrm{m}}} \tag{11}$$

where η_t is the turbulent diffusivity, σ_t is the Prandtl/Schmidt number and set to 0.75, $a_{k,I}$ is the acceleration of phase k, and d_k is the bubble and particle diameter of phase k. f_{drag} is the drag force function for the secondary phase. The main settings of the RSM, VOF, and TFM models applied herein are summarized in Table 1, and more details of these models can be found in the literature.[55,56]

Figure 1 illustrates the present Eulerian−Eulerian simulation strategy. First, the multiphase flow field of the water−air is established. The VOF model was used to capture the phase interface of water and air. Next, the particle phases were introduced into the calculation domain. Herein, the mixture multiphase model replaced the VOF model to predict both the water−air core interface and the particle flow under the Eulerian frame. In this Eulerian−Eulerian method, particles of different diameters were treated as different phases and their properties were described through the kinetic theory of granular flow. The phase volume fraction at the inlet was defined as the feed particle size distribution measured by a Malvern Mastersizer 3000 particle size analyzer.

Note that the particle−particle interaction was not calculated in the mixture model herein. This omission is

Table 1. Main Settings of the RSM, VOF, and TFM Models

| item	value
	RSM Model
pressure strain model	linear pressure strain
near wall treatment	standard wall function
Reynolds stress options	wall reflection effects
	VOF Model
phase interface modeling	dispersed
volume fraction formulation	implicit formulation
spatial discretization schemes for volume fraction	QUICK
	TFM model
continuity and momentum equation	mixture[57]
slip velocity	algebraic[57]
drag model	Schiller−Naumann correlation (air−liquid),[58] Gidaspow model (particle−liquid)[59]
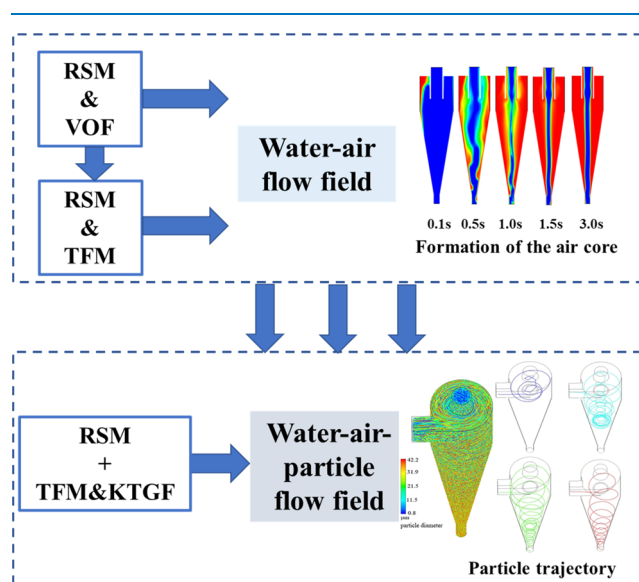
Figure 1. Eulerian−Eulerian simulation strategy.

acceptable in the feed SC range of this study as the particle−particle interaction is most influential when the SC is very high, as several studies have reported for their own applications.[60−64] Herein, a combination of the second-order upwind/QUICK discretization scheme, PRESTO pressure interpolation scheme, and SIMPLE pressure−velocity coupling algorithm was adopted as the optimal numerical calculation method. The unsteady solver was used as the convergence strategy, with a time step of 5×10^{-4} s, and the accuracy of the convergence criterion was set to 1×10^{-4}. The commercial package FLUENT was used as the CFD solver.

2.1.2. Simulation Conditions. The geometrical structures and computational grids of the MnO_2 hydrocyclones are shown in Figure 2, the details of which are listed in Table 2. A mesh independence study was conducted for hydrocyclone A with three different meshes (63 994, 140 760, and 278 070 hexahedral grids) as examples. The results of the axial and tangential velocities of different meshes at a height of 272 mm from the spigot bottom are compared in Figure 2b. The results of the 140 760 and 278 070 grids are quite similar. Therefore, the mesh of 140 760 grids was applied for the simulation.

The pressure-outlet boundary condition was used at the two outlets (spigot and vortex finder), where the pressure was set
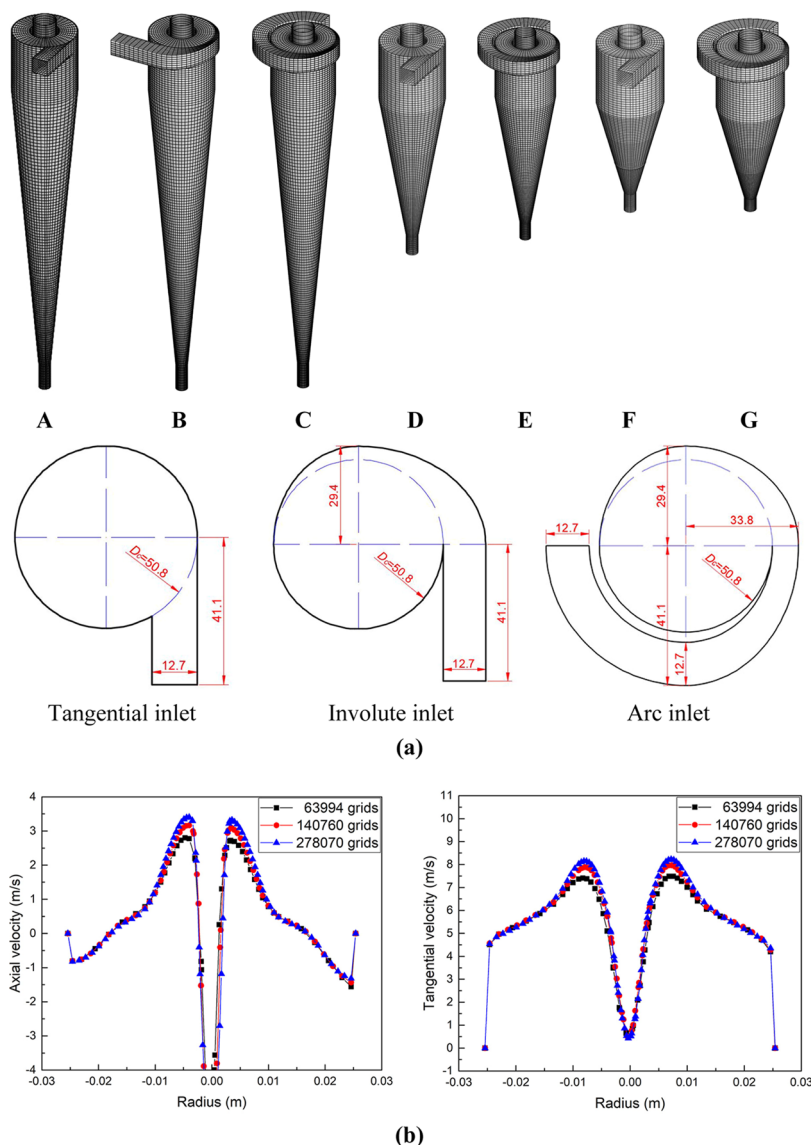
Figure 2. (a) Schematic of the geometrical structures and computational grids of the MnO$_2$ hydrocyclones: tangential inlet types (A, D, F), involute inlet type (B), and arc inlet types (C, E, G); cone angles of 10° (A, B, C), 20° (D, E), and 30° (F, G) and (b) mesh independence analysis for hydrocyclone A in terms of axial and tangential velocities at a height of 272 mm from the spigot bottom.

Table 2. Structural Variables of the MnO$_2$ Hydrocyclone

parameter	symbol	value
cylindrical body diameter	D_c	50.8 mm
inlet size	D_i	12.7 mm × 12.7 mm
inlet type		tangential (A, D, and F), involute (B), and arc (C, E, and G)
vortex finder diameter	D_o	18 mm
vortex finder thickness	w	2 mm
spigot diameter	D_u	9 mm
vortex finder length	L_o	25.4 mm
cylindrical part length	L_c	50.8 mm
cone angle	γ	10° (A, B, and C), 20° (D and E), and 30° (F and G)

to 1 atm. A velocity-inlet boundary condition was applied at the inlet. The inlet velocity was 4.95 m/s, and the MnO$_2$

particles (density = 5030 kg/m^3) were homogeneously injected into the hydrocyclone with a feed SC of 2.5, 5, 10, or 15 wt %. Their particle size distribution is shown in Figure 3a. Interestingly, the physical properties of the MnO$_2$ particles are similar to those of magnetite particles reported in the dense medium cyclone,[14,53,65] and a similar fluidization treatment for the particle phases has been used herein (Section 2.1). The particle classification target was set to 5 μm, as required for the MnO$_2$ particle process, i.e., particles <5 μm were to be eliminated from the underflow, and particles >5 μm were to be recovered from the underflow. Particle injection began at a physical time of 3.5 s when a stable water−air core flow field was achieved. The simulation was stopped after another physical time of 3.5 s as the flow rate was stable. The mass balance of the water phase and the flow rate of the 5 μm particles at the spigot were monitored to judge the stability, as reported previouly[66] Data from the simulation of hydrocyclone A operated with a 5 wt % feed slurry are shown in Figure 3b,c as an example. The following results and discussion are based
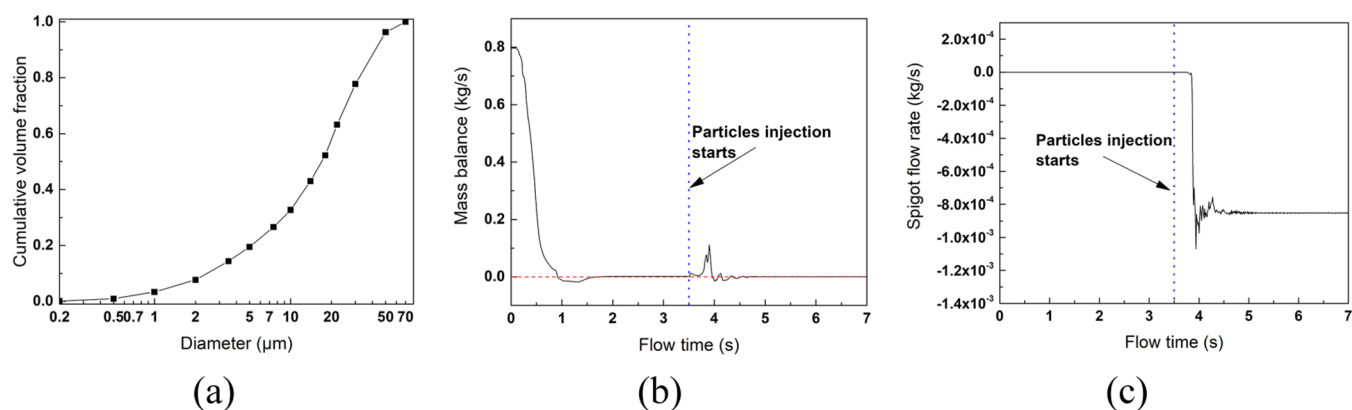
Figure 3. (a) Particle size distribution of MnO_2 feed, (b) mass balance of the water phase, and (c) flow rate of the 5 μm particle phase at the spigot.
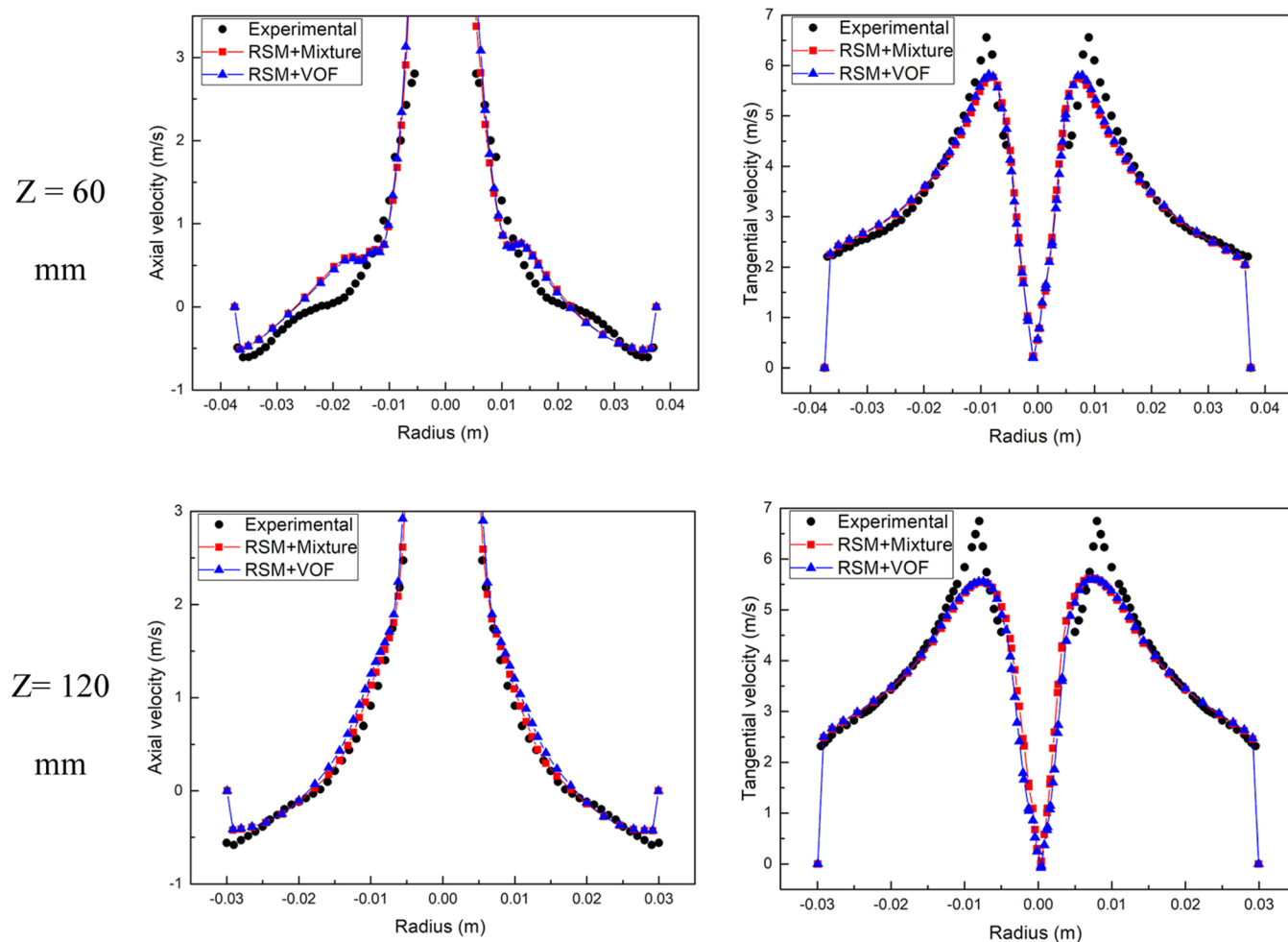

Figure 4. Comparison of simulation and reference axial tangential velocity profile measurements at 60 and 120 mm from the top wall.

on the time-averaged data of the last 1 s of physical time during the simulation.

2.1.3. Model Validation. It is important to validate the simulation model to ensure the reliability of the method. In the case of water−air multiphase flow, validation was performed by comparing our simulation results with the experimental measurements of Hsieh[67] in a 75 mm hydrocyclone (Figure 4), which has been widely applied for model validation.[11,60,64] Importantly, the experimental data are symmetrical, as the data are provided as the mean values of two sides. It was apparent

that both the VOF and mixture multiphase models reliably predicted the fluid field of the water and air cores. Good agreement between the simulation results and reference measurement data demonstrates the effectiveness of our simulation method to build a reliable initial flow field before introducing particle phases, though there is a gap between the experimental and simulation results at the radius of −0.01 and 0.01 mm especially in the tangential velocity. It was because of the unsteady state of the air core in the center of the hydrocyclone.
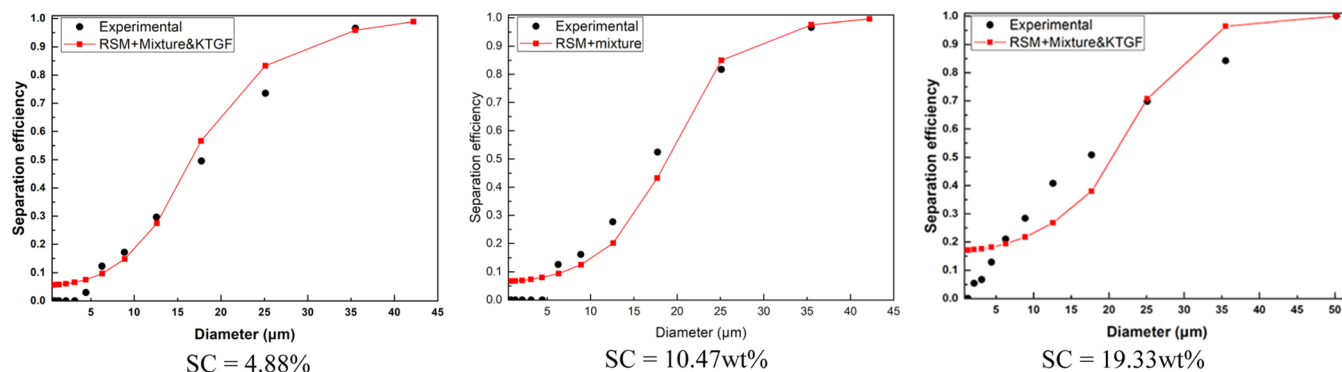
SC = 4.88% SC = 10.47wt% SC = 19.33wt%

Figure 5. Separation efficiency curve comparison.

1-tank
2-valve
3-centrifugal pump
4-regulating tank
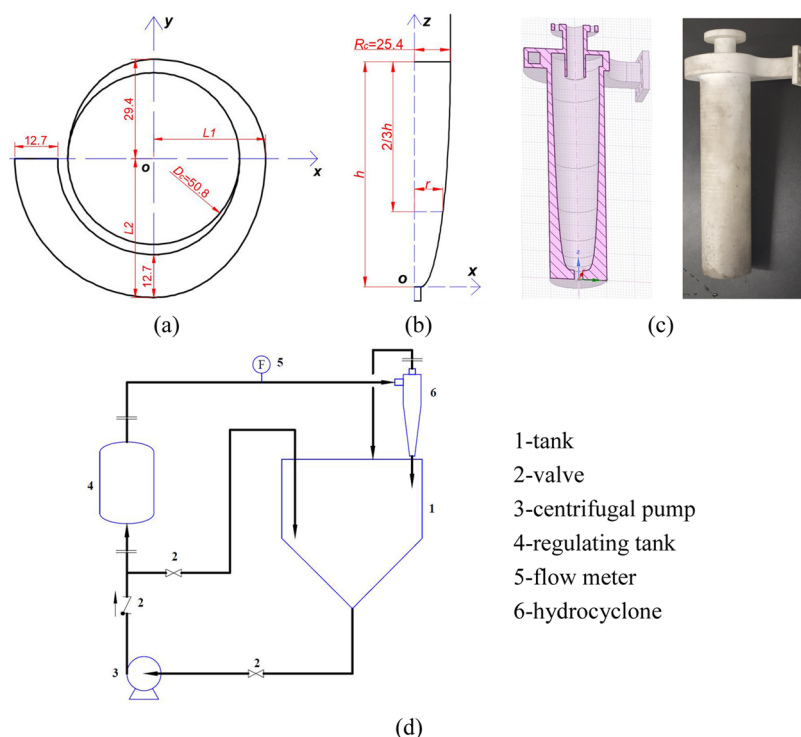5-flow meter
6-hydrocyclone

(a) (b) (c)

(d)

Figure 6. Geometrical design of the novel hydrocyclone (unit: mm): (a) arc inlet section, (b) curve of the conical section, (c) 3D model and photo, and (d) experimental flow sheet.

In the case of water−air−particle multiphase flow, the separation efficiency for particles of a certain size was defined as the recovery ratio of these particles from the spigot and calculated from the mass flow rate at every outlet plane. Figure 5 shows our simulated separation efficiency curve and the experimental results of Hsieh[67] in a 75 mm hydrocyclone with limestone of different solid contents. The simulation results provide a reasonable prediction of the experimental particle partition, though the prediction accuracy of the model for the separation efficiency is reduced with the increase of the solid content. But it still can predict the trend of the separation efficiency of different particle sizes. However, the separation efficiency of particles smaller than 5 μm in the experiment is zero, which is different from the results of the simulation. It might be because the concentration of small particles is too low to measure by the experimental instrument. The same comparison between the predicted and experimental results were also in Hsieh's research.[67] Additionally, the predicted pressure drop of 42 102 Pa is close to the experimental result

of 46 700 Pa. Thus, the CFD methods adopted herein are reliable for multiphase simulation in hydrocyclones.

2.2. Experimental Methods. *2.2.1. Experimental Materials.* The feed slurry for the hydrocyclone was prepared by mixing MnO_2 powder and tap water with a slurry SC of 10 wt %. MnO_2 powder was provided by the Red Star Chemical Group Co., Ltd (Tongren, Guizhou, China) with a density of 5030 kg/m^3, and its particle size distribution is shown in Figure 3a.

2.2.2. 3D-Printed Hydrocyclone and the Experimental Procedure. Conventional and novel hydrocyclones were used in the experimental separation performance test. The conventional hydrocyclone has the same geometrical structure as hydrocyclone D (Figure 2a). The novel hydrocyclone designed based on this work and a previous study shares the same main body, inlet, vortex finder, and spigot diameters; however, it was optimized for the inlet type and cone section. The novel hydrocyclone had an arc inlet that can be described using the elliptic curves shown in Figure 6a−c, where L_1 = 32.0 mm and
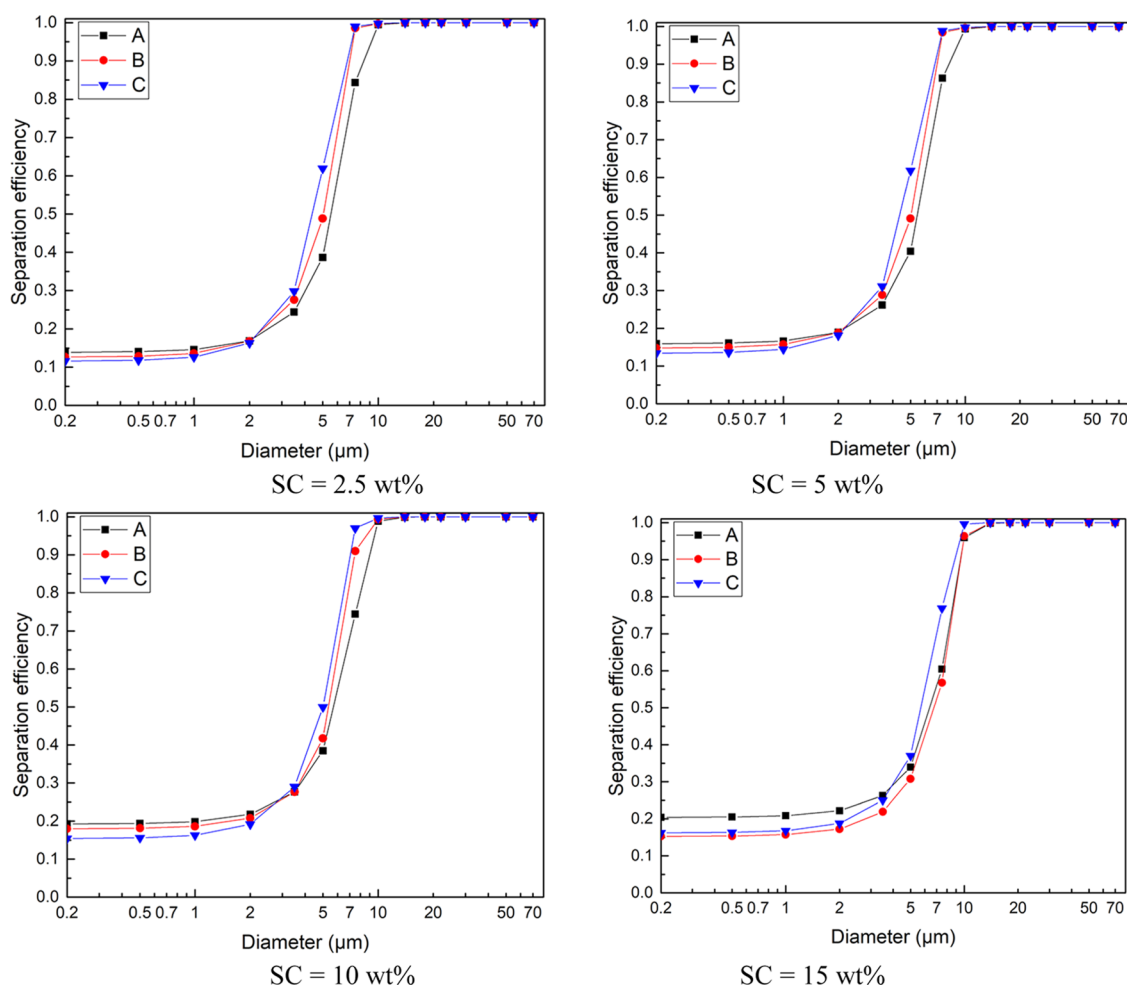
Figure 7. Separation efficiency of MnO$_2$ hydrocyclones with different inlet types: tangential (A), involute (B), and arc (C) inlets with a 10° cone angle.

L_2 = 50.3 mm are the short and long axes of the inlet elliptical arc, respectively. Additionally, the cone section shape is given by the function $z = a(x - D_u/2)^n$, which can be deduced as $a = h/(D_c/2 - D_u/2)^n = 2.10 \times 10^{-4}$ and $n = \log(1/3)/\log(h/(r - D_u/2)) = 4.52$.

The conventional hydrocyclone was fabricated using conventional machining methods, whereas the optimized one was built using selective laser sintering 3D printing with nylon as the material of choice.

The flow sheet of the separation performance experiment is shown in Figure 6d. A centrifugal pump powers the flow of the system. The feed slurry is pumped by the centrifugal pump through the flowmeter, hydrocyclone, and bypass pipe, and returned to the tank. The circulating flow operation prevents the particles in the feed slurry from precipitating and maintains uniform dispersion. The overflow and underflow samples are obtained at the vortex finder and spigot, respectively, after the flow rate is stable at the desired value corresponding to an inlet velocity of 4.95 m/s. The particle size distribution of the overflow/underflow products is measured using a Malvern Mastersizer 3000 particle size analyzer. The morphology of the samples is analyzed using scanning electron microscopy (SEM, FEI Quanta 250). The SC of the overflow/underflow slurry is measured using the gravimetric method after filtration and drying.

To evaluate the separation performance, the fine particle (≤ 5 μm) removal efficiency (C_f) and coarse particle (>5 μm) recovery efficiency (C_c) are defined as follows

$$C_f = \frac{(1 - R_f)SC_o \sum_{d \leq 5\mu m} p_{d,o}}{(1 - R_f)SC_o \sum_{d \leq 5\mu m} p_{d,o} + R_f SC_u \sum_{d \leq 5\mu m} p_{d,u}} \tag{12}$$

$$C_c = \frac{R_f SC_u \sum_{d > 5\mu m} p_{d,u}}{(1 - R_f)SC_o \sum_{d > 5\mu m} p_{d,o} + R_f SC_u \sum_{d > 5\mu m} p_{d,u}} \tag{13}$$

where $p_{d,o}$ and $p_{d,u}$ are the particle size distribution data and R_f is the slurry split ratio, which is calculated as follows

$$R_f = \frac{SC_u - SC_o}{SC_f - SC_o} \tag{14}$$

3. RESULTS AND DISCUSSION

3.1. Effects of Arc Inlet. *3.1.1. Effect of Arc Inlet on Separation Performance.* Figure 7 presents the separation efficiency of three hydrocyclones with different inlets (A, tangential; B, involute; and C, arc; the details are presented in Figure 2 and Table 2). Overall, the novel arc inlet (C) provided better particle classification performance than the
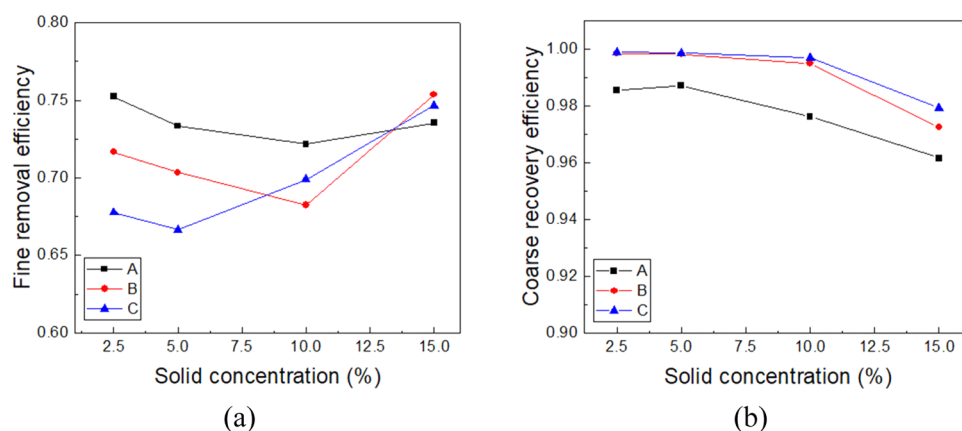
Figure 8. Classification performance of (a) underflow C_f and (b) underflow C_c: tangential (A), involute (B), and arc (C) inlets with a 10° cone angle.
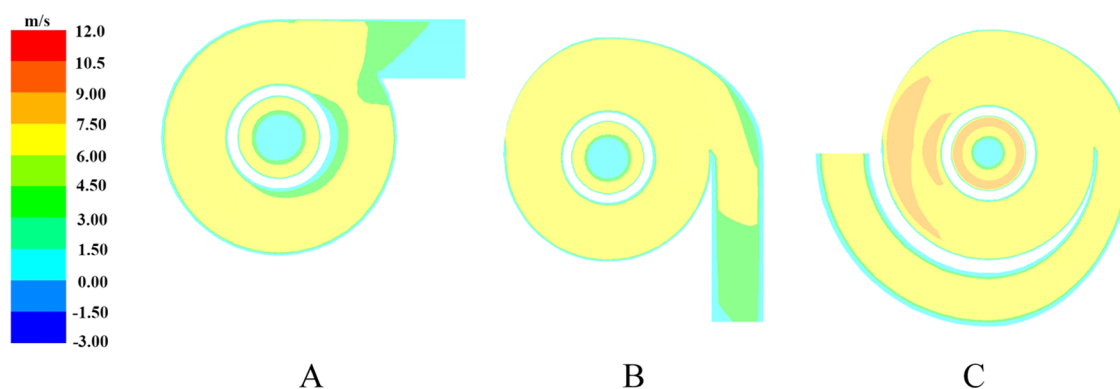

Figure 9. Inlet section tangential velocity profile (pure water feed): tangential (A), involute (B), and arc (C) inlets with a 10° cone angle.

traditional tangential (A) and involute (B) inlets. A high separation efficiency was achieved for particles >5 μm in the hydrocyclone with the arc inlet (C). Furthermore, the arc inlet hydrocyclone provided a low separation efficiency for particles <2 μm. The ultrafine particle removal performance of the arc inlet was better than that of the tangential inlet, and its separation efficiency for coarse particles was higher than that of the involute inlet with a greater feed SC (up to 15 wt %). The separation efficiency for ultrafine particles (0.2 μm) was reduced from 0.20 (A) to 0.16 (C), and the separation efficiency for coarse particles (7.5 μm) was improved from 0.57 (B) to 0.77 (C).

The separation performance was also interpreted through the analysis of C_f and C_c (Figure 8). C_f ($\leq$5 μm) and C_c (>5 μm) were used to evaluate the partition of the particles at the vortex finder and spigot, respectively. Under a low feed SC, the tangential inlet hydrocyclone design exhibited a higher C_f than the arc inlet design. This was attributed to the contribution of slightly larger fine particles (2−5 μm). As the feed SC increased, the C_f values of the different inlets approached each other. In contrast, the C_c of the arc inlet maintained a stable advantage over tangential and involute inlets under various feed SCs. Overall, the arc inlet provided the best performance over the entire range of feed SCs.

3.1.2. Dynamic Analysis of the Effect of the Inlet. Figure 9 shows the tangential velocity profile at the hydrocyclone inlet section. The arc inlet (C) created a much stronger centrifugal force field with a higher tangential velocity than the tangential (A) or involute (B) inlets. This stronger centrifugal force field

may enhance classification, which corresponds to the various force states of particles of different sizes.

Figure 10 presents the radial acceleration distribution of certain particle phases at 6.5 mm from the top wall of the hydrocyclones with different inlet types (A, B, and C). The sum of the pressure gradient and drag force in the radial direction acts as a centripetal force that supports particle motion in the orbits. Thus, radial acceleration is extracted from the time-averaged fluid field as the sum of the pressure gradient and drag acceleration (force/mass). As the particle diameter has no impact on the pressure gradient acceleration (force/mass), the difference between the different particle phase accelerations can be mainly attributed to the drag acceleration (force/mass). The radial acceleration of particles quickly reduces to 0 at the radii of 0.0254 and 0.09 m because of the effect of the hydrocyclone wall and vortex finder wall, respectively.

The hydrocyclone with the arc inlet (C) exhibited a stronger centrifugal phase separation effect (Figure 10, drag force is defined based on the relative motion of the phases). The difference in radial acceleration between particle phases was the most significant in the arc inlet (C). This explained its higher classification sharpness, as the magnitude of the radial acceleration disparity reflects the particle phase classification effect. Furthermore, the stronger separation force affects particles with a size of 2−5 μm in a manner similar to how the coarse particles are affected, although these particles only comprise the coarse portion of the fine particle region. This agreed to some extent with the inferior fine particle removal of
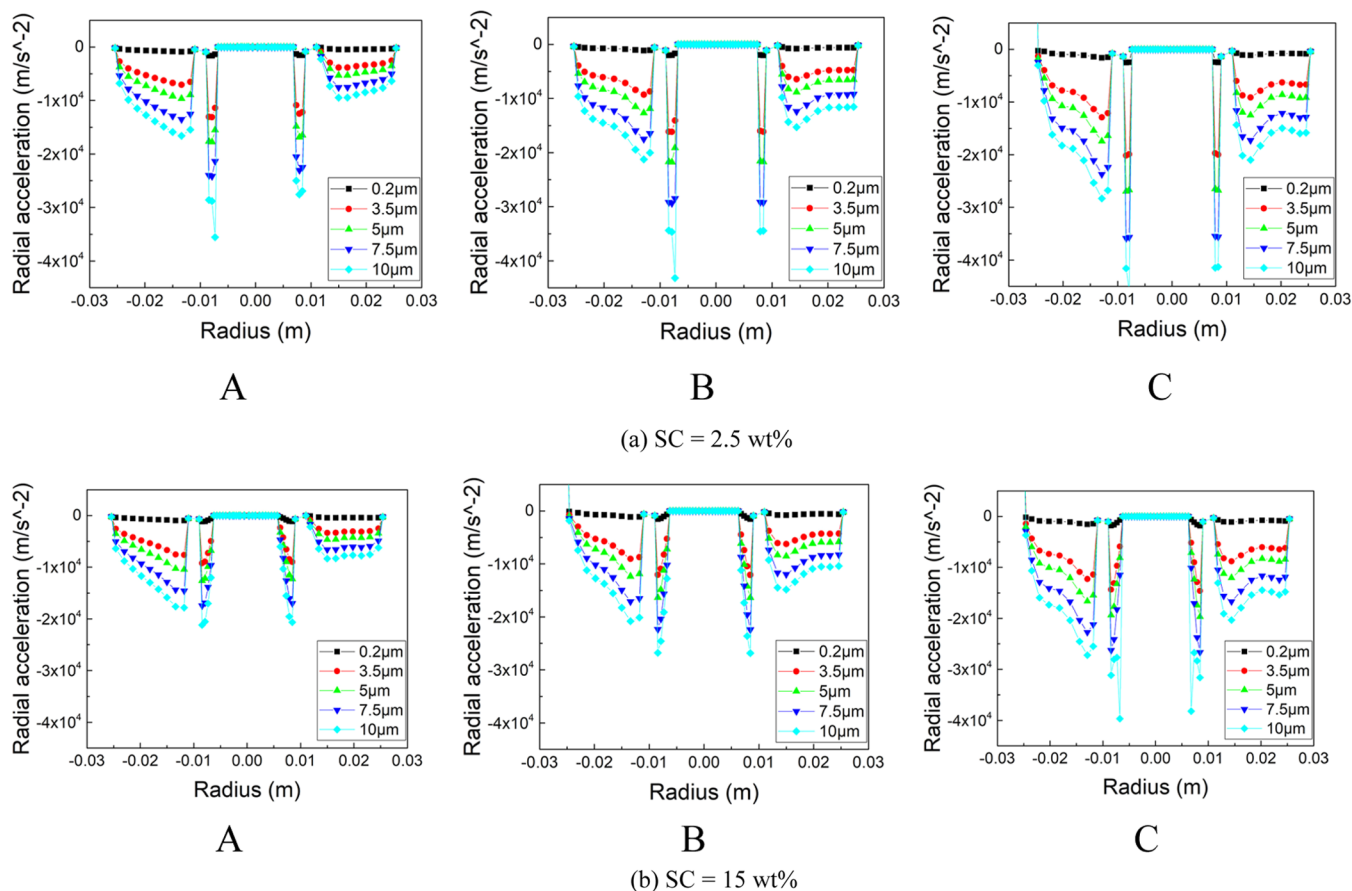
(a) SC = 2.5 wt%

(b) SC = 15 wt%

Figure 10. Particle phase radial acceleration distribution at 6.5 mm from the top wall with (a) SC = 2.5 wt % and (b) SC = 15 wt %: tangential (A), involute (B), and arc (C) inlets with a 10° cone angle.

the arc inlet. In addition, the feed SC had little effect on radial acceleration; therefore, it may not affect the classification in the inlet section (Figure 10).

Stronger turbulence fluctuation can enhance the stochastic motion of particles,[11] such as the ultrafine particles (<2 μm) in this study. This type of stochastic motion can weaken the classification effect provided by the centrifugal field. Thus, a lower turbulence intensity is beneficial to hydrocyclone classification as it represents the ratio of turbulence fluctuating velocity to time-averaged velocity. The turbulence intensity in the involute (B) and arc (C) inlet sections was generally lower than that in the tangential (A) inlet, especially in the inner part (inside the red dashed circle, Figure 10). Therefore, the involute and arc inlets were favorable for reducing the particle misplacement caused by turbulence fluctuations. In contrast, the feed SC had little influence on the turbulence intensity profile (Figure 11a,b).

Previous experimental and numerical studies[42,68] have highlighted the effect of the initial position of a particle on its motion behavior. When the liquid−solid slurry is injected into the hydrocyclone inlet at a certain speed, two basic flow patterns are formed, namely, an inner spiral and outer spiral flow. The outer spiral flow moves downward and toward the wall, while the inner spiral flow moves upward and toward the center. After entering the hydrocyclone, the area close to the inner wall of the inlet is in the inner spiral flow area, and the area close to the outer wall of the inlet is in the outer spiral flow area. while the middle area is defined here as the transition zone. Therefore, the inlet cross-sectional area is divided into three rectangular parts (areas I, II, and III) from the center to the wall of the hydrocyclone (Figure 12a). Particles approaching area III are more likely to be captured by the outer vortex and delivered to the underflow. In a similar observation, those particles approaching from area I have a higher probability of being transported to the overflow vortex finder. Therefore, coarse and fine particles should be in areas III and I, respectively, during preclassification. Based on the analysis of the particle phase profile at the inlet cross-sectional area (Figure 12b), the arc inlet (C) was found to provide this desirable state.

As illustrated in Figure 12b, the particle phase volume fraction distribution of the tangential (A) and involute (B) inlets showed more homogeneous characteristics from areas I to III. However, the volume fraction profile of the arc inlet (C) exhibited a different trend. At the arc inlet, more ultrafine particles were distributed into the inner section, as the volume fraction of particles with a size of 0.2 μm in area I was much higher than that in area III. The volume fraction distributions of the fine (3.5 μm) and target cut size (5 μm) particles in the arc inlet were similar to those in the tangential and involute inlets. The volume fraction of the coarser particles (7.5 μm) increased considerably with the increase in the distance to the inner side, which resulted in a higher phase concentration in outer area III of the arc inlet. These phase distribution characteristics at the arc inlet became more apparent as the particle size increased, as shown for the volume fraction distributions of 10 and 70 μm particles (Figure 12b). Furthermore, the particle phase preclassification effect of the
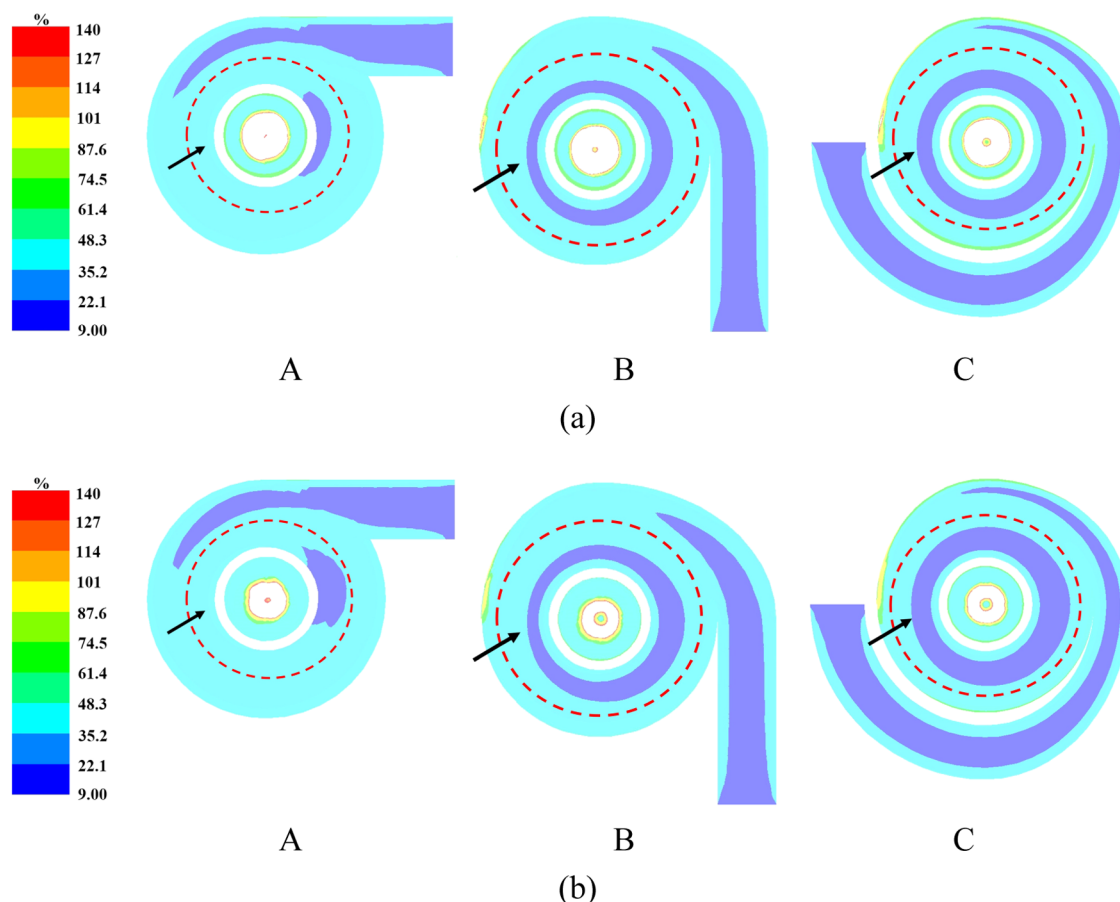
Figure 11. Inlet section turbulence intensity profile for various structures with (a) SC = 2.5 wt % and (b) SC = 15 wt %: tangential (A), involute (B), and arc (C) inlets with a 10° cone angle.

arc inlet improved the separation sharpness, whereas the other two inlet structures did not provide such an effect. This preclassification effect of the arc inlet is also a favorable factor for reducing the phase entrainment of coarse particles into fine particles during actual operation.[12,69]

The preclassification ratio (E_{pc}) is defined as the split ratio of a certain particle phase at the inner (area I), central (area II), or outer (area III) sections of the inlet cross-sectional area

$$E_{pc} = \frac{F_{k,c}}{F_{k,in}} \tag{15}$$

where $F_{k,c}$ and $F_{k,in}$ represent the volume flow rates of the kth particle phase at a certain inlet cross-sectional area and the inlet, respectively.

Figure 13 illustrates the E_{pc} values of the hydrocyclones with inlets of A, B, and C. The arc inlet (C) achieved a higher E_{pc} of coarse particles in outer area III and fine particles in inner I and central area II. In addition, increasing the feed SC made had little effect on the preclassification at the inlet section, as the volume fraction distribution (Figure 12b) and E_{pc} (Figure 13) exhibited no significant changes.

The above analysis demonstrates the extra separation contribution of the arc inlet, as the preclassification effect was achieved via extra centrifugal separation in the arc path. It can be inferred that such an effect cannot be achieved in the other two conventional designs by simply extending the inlet length, as centrifugal effects are not provided by their straight inlet pipes.

Although an increased feed SC had no significant effect on the inlet section fluid field or particle preclassification, the separation sharpness exhibited clear variation with increasing feed SC (Figure 7). Moreover, the separation sharpness correlated strongly with the fluid field in the other parts of the hydrocyclone, such as the conical section, which considerably influences separation performance.[43,44,46] This and the combined optimization design for realizing better performance are discussed in the following section.

3.2. Effect of Cone Angle. *3.2.1. Effect of Cone Angle on Separation Performance.* Figure 14 shows the separation efficiency of the various studied hydrocyclones (A, C, D, E, F, and G). An increase in the cone angle considerably improved the removal of fine particles (≤5 μm); however, the recovery of coarse particles decreased rapidly in the tangential inlet hydrocyclones. The larger cone hydrocyclones with an arc inlet did not have this drawback, and achieved superior general classification performance. Under low feed SCs (2.5 and 5 wt %), the 20° cone angle hydrocyclone with an arc inlet (E) exhibited a higher C_c than hydrocyclones with a tangential inlet (A, D, and F). Furthermore, this hydrocyclone maintained a high C_f. The hydrocyclone with a cone angle of 30° and an arc inlet (G) exhibited further improved fine particle removal, while the underflow separation efficiency of the finest particles (0.2 μm) was reduced to <0.04. However, its performance in the coarse particle region was weaker than the performance of E. In general, increasing the feed SC deteriorated the performance of the hydrocyclones. Hydrocyclones with larger cone angles exhibited superior fine particle removal perform-
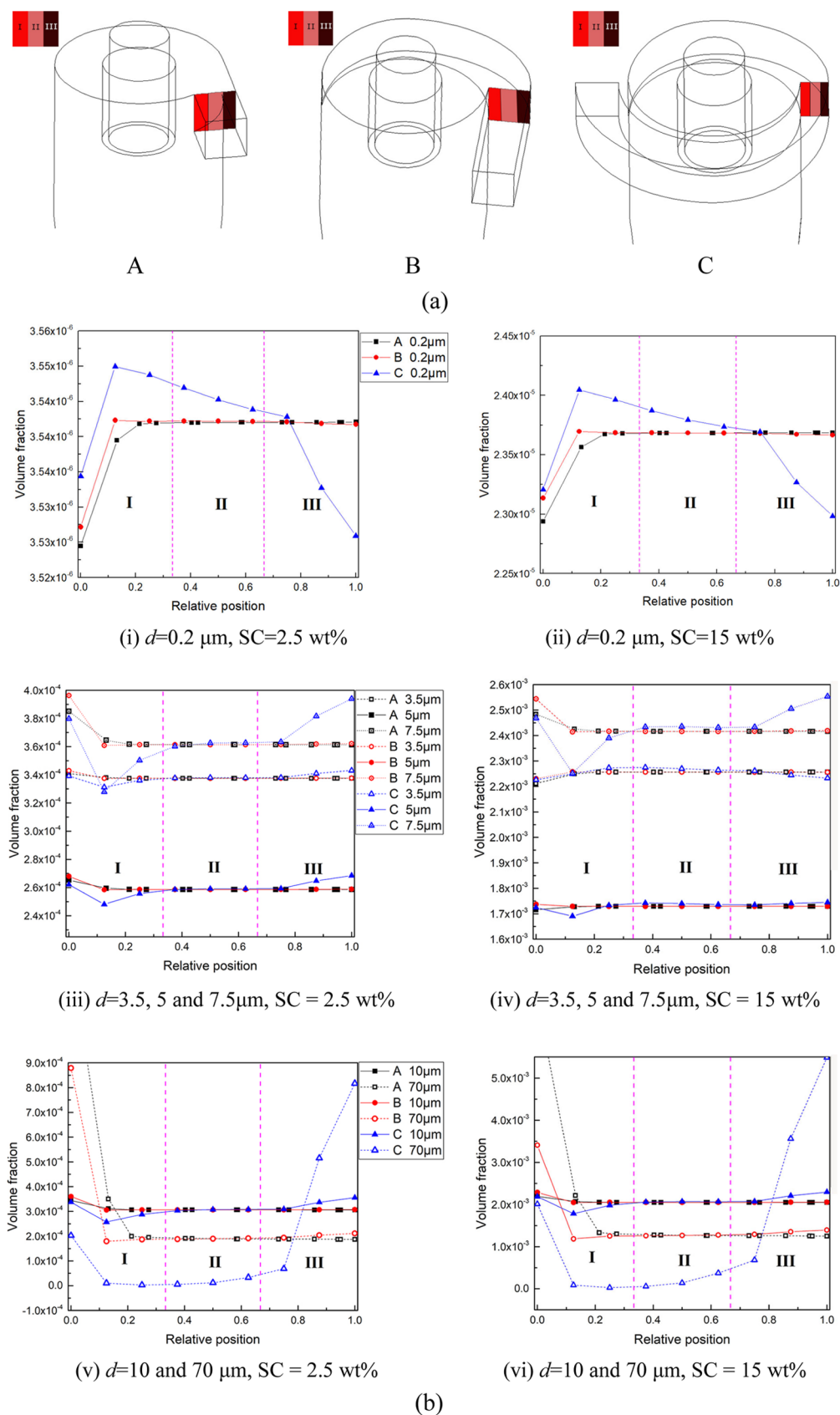
(a)

(i) d=0.2 μm, SC=2.5 wt%

(ii) d=0.2 μm, SC=15 wt%

(iii) d=3.5, 5 and 7.5μm, SC = 2.5 wt%

(iv) d=3.5, 5 and 7.5μm, SC = 15 wt%

(v) d=10 and 70 μm, SC = 2.5 wt%

(vi) d=10 and 70 μm, SC = 15 wt%

(b)

Figure 12. Particle phase volume fraction distribution at the inlet section. (a) Inlet plane schematic and (b) particle phase volume fraction distribution: tangential (A), involute (B), and arc (C) inlets with a 10° cone angle.

ance than those with smaller cone angles but did not show better resistance to the decrease in C_c.

As shown in Figure 15a,b, the arc inlet provided better C_c than the tangential inlet. Hydrocyclones with a tangential inlet
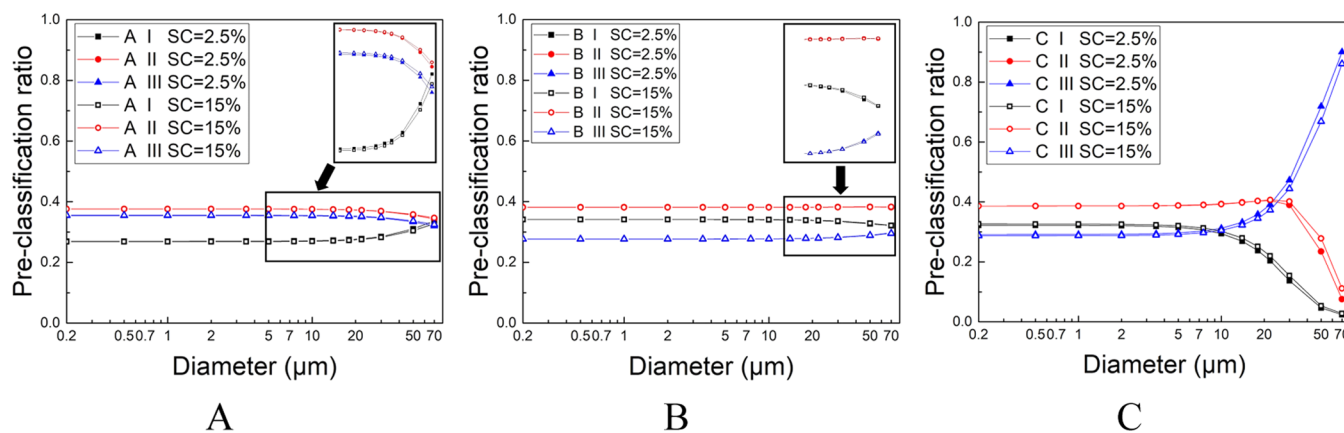
Figure 13. Preclassification ratio for different hydrocyclones at SCs of 2.5 and 15 wt %: tangential (A), involute (B), and arc (C) inlet with a 10° cone angle.
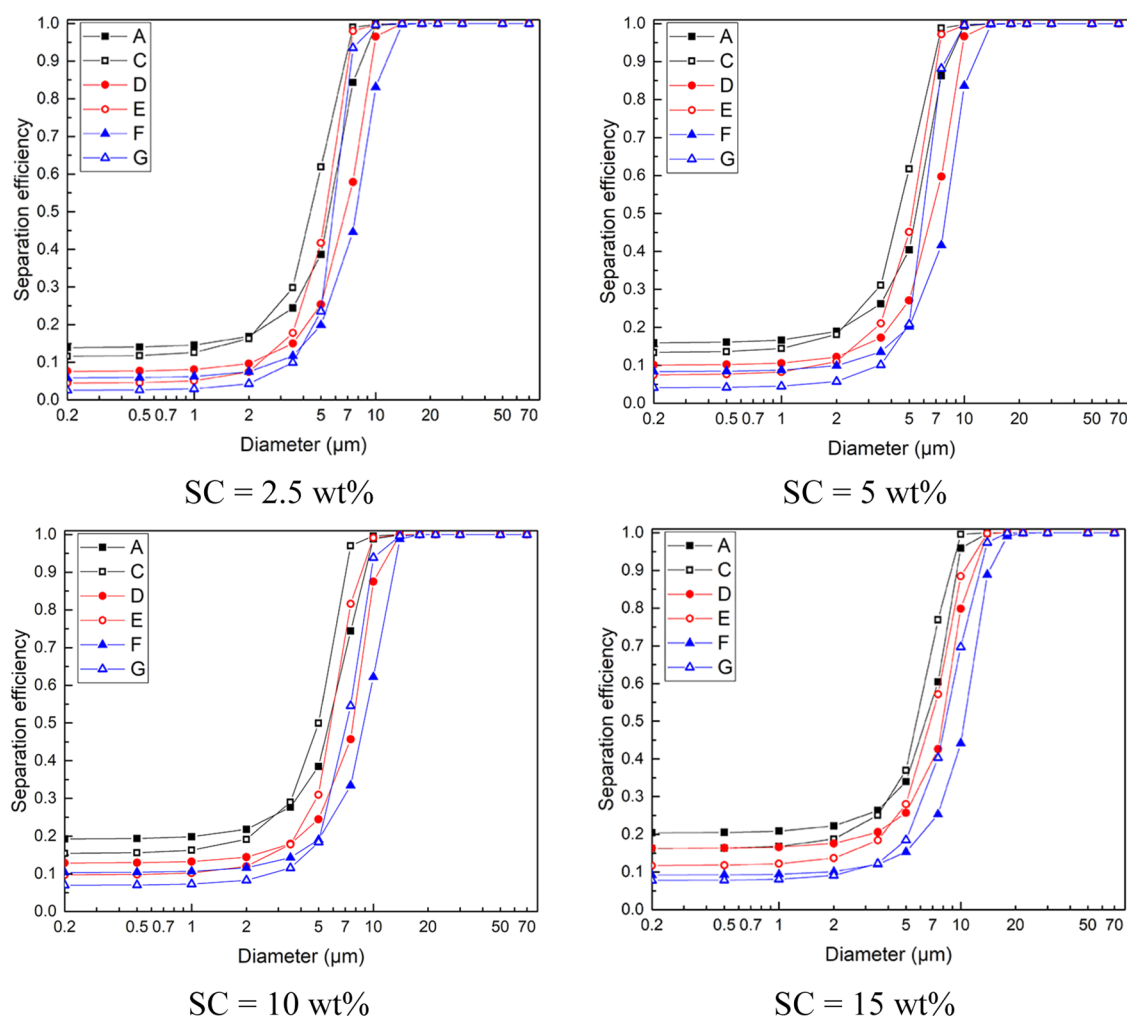

Figure 14. Separation efficiency of MnO$_2$ hydrocyclones with various inlets and cone angles: tangential (A, D, and F) and arc (C, E, and G) inlets with cone angles of 10° (A and C), 20° (D and E), and 30° (F and G).

and 10 and 20° cone angles showed better C_f than the arc inlet under a low SC. However, hydrocyclone G with a 30° cone angle and an arc inlet exhibited the best C_f and C_c under a low SC. Comprehensively considering the removal of fine particles and recovery of coarse particles, the arc inlet combined with a 30° cone angle design is believed to be optimal under a low SC. Hydrocyclone G with an SC of 2.5 wt % provided the best

classification performance (C_f = 0.89 and C_c = 0.99). With the increase in feed SC, the general separation performance of all hydrocyclones decreased, but the arc inlet hydrocyclones still exhibited relatively better performance than the tangential ones. If a higher feed SC is inevitable, the arc inlet combined with a 20° cone angle design may be an appropriate alternative for a wide range of operating feed SCs.
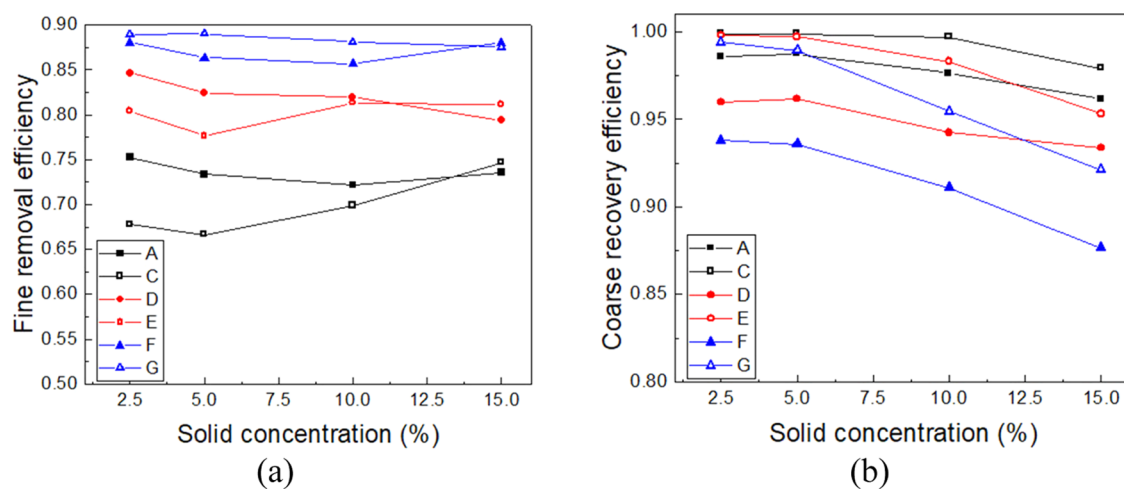
Figure 15. Classification performance of MnO_2 hydrocyclones with various inlets and cone angles: (a) underflow C_f and (b) underflow C_c: tangential (A, D, and F) and arc (C, E, and G) inlets; cone angles of 10° (A and C), 20° (D and E), and 30° (F and G).
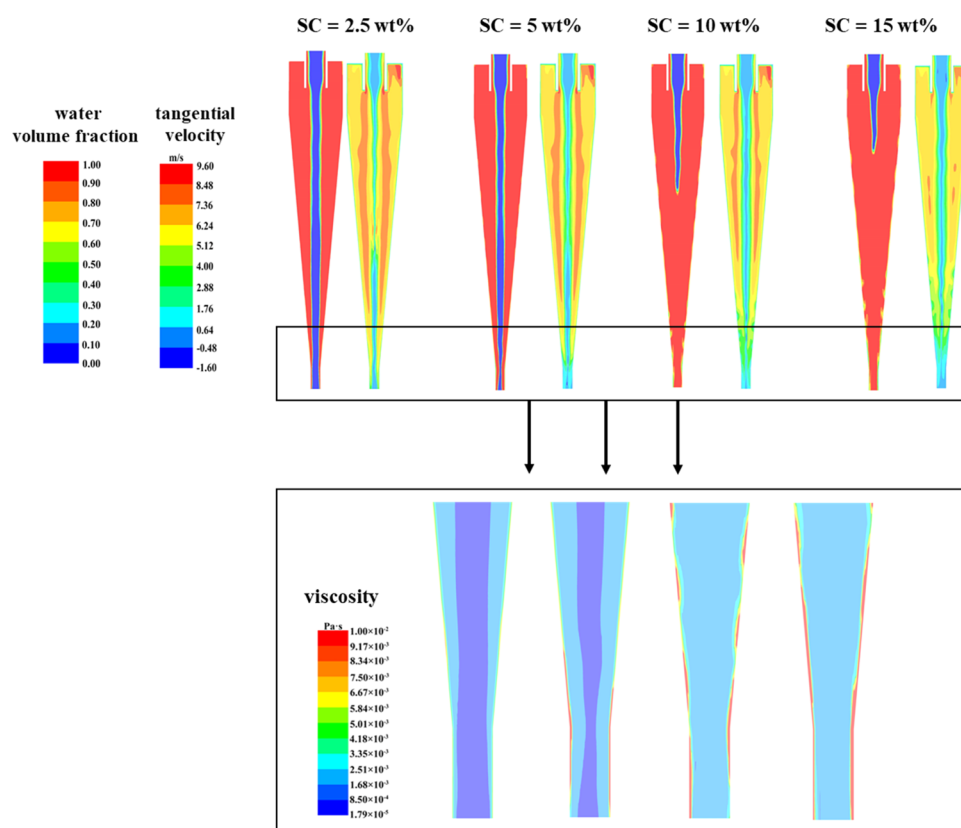

Figure 16. Fluid field in hydrocyclone (C) under various feed SCs.

3.2.2. Dynamic Analysis of the Effect of Cone Angle. Figure 16 shows the effect of feed SC on the fluid field in hydrocyclone C. The swirling characteristics of the hydrocyclone flow field are significantly weakened with increasing SC, as the air core disappears in the cone section and tangential velocity decreases. This deterioration of the swirling effect can be attributed to the loss of momentum of the fluid, which can be explained by the variation of fluid properties. The viscosity considerably increases with increasing SC, especially in the region near the wall. As viscosity represents the internal friction in the fluid, the loss of momentum of the fluid can be attributed to the increased viscosity, which has also been

mentioned in the literature.[60] Considering the fluid field discussed in Section 3.1.2, the variation in SC has a much greater effect on the cone section than the inlet section. Thus, the effect of SC on separation performance can be attributed to a change in the fluid field in the conical section.

The pressure gradient acceleration was much lower than the drag acceleration in the global range, except at the wall (Figure 17a). Thus, the drag acceleration had a greater influence on the motion behavior of particles, as discussed in the inlet section. Figure 17b shows that hydrocyclones with an arc inlet (C or G) create a much stronger drag acceleration field in the global range than the tangential ones (A or F), and the larger cone
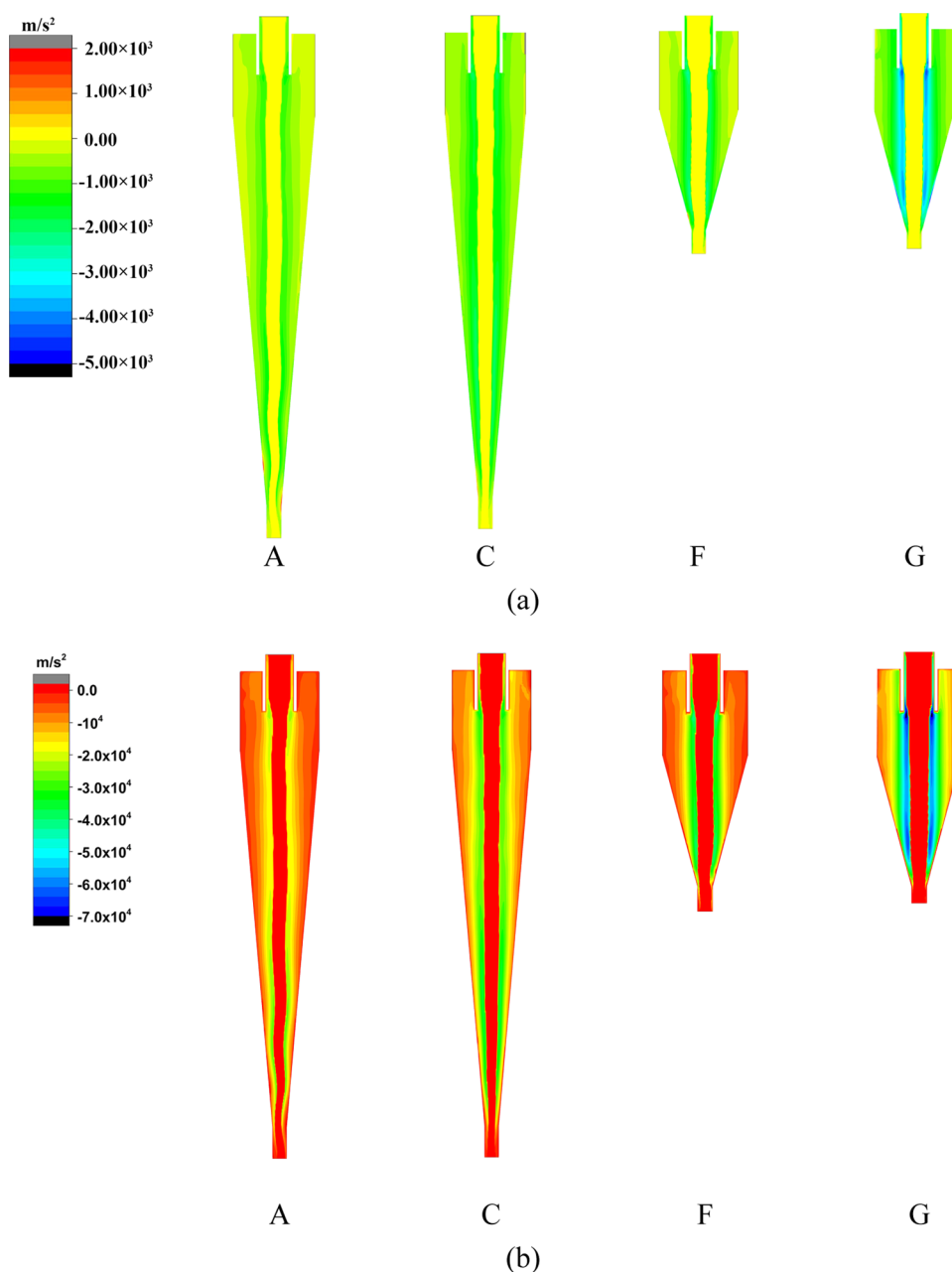
Figure 17. Radial pressure gradient force acceleration (a) and drag force acceleration profiles (b) of the 5 μm particle phase at SC = 5 wt %: tangential (A and F) and arc (C and G) inlets; cone angles of 10° (A and C) and 30° (F and G).

angle has a similar effect. Drag acceleration represents the relative motion between the particle phase and water; therefore, the arc inlet and larger cone angle provide a stronger separation driving force.

Figure 18 presents the detailed radial acceleration distribution of certain particle phases at the center-height position of the cone section. Hydrocyclone with an arc inlet (C, E, or G) maintained higher radial acceleration than the others (A, D, or F) under all feed SCs evaluated. In addition, in hydrocyclones with an arc inlet, the radial acceleration was more greatly enhanced with increasing cone angle than in those with a tangential inlet. This demonstrates the contribution of optimal inlet design to the improvement in the conical section fluid field.

As Figure 15 shows, the effects of cone angle on C_f and C_c are quite different. With increasing cone angles, the magnitude of radial acceleration increased (Figure 18), indicating a higher kinetic energy and motion speed of the particle phase. As the motion speed of the particle phase increases, the particles generally spend less time in the device, yielding a shorter residence time. Therefore, the larger cone angle provides enhanced C_f as the time-accumulative separation effect to the underflow is weakened. Considering the inlet section design, the different inlets provide different performances with variation in the cone angle. In the hydrocyclone with a traditional tangential inlet, the C_c deteriorates as the cone angle increases. In the hydrocyclone with an arc inlet, the increase in radial acceleration and the preclassification effect help maintain C_c. Thus, increased C_f and C_c can be achieved by combining an arc inlet and a large cone angle.

The effect of feed SC on the hydrocyclone classification performance was analyzed. An increase in SC resulted in higher
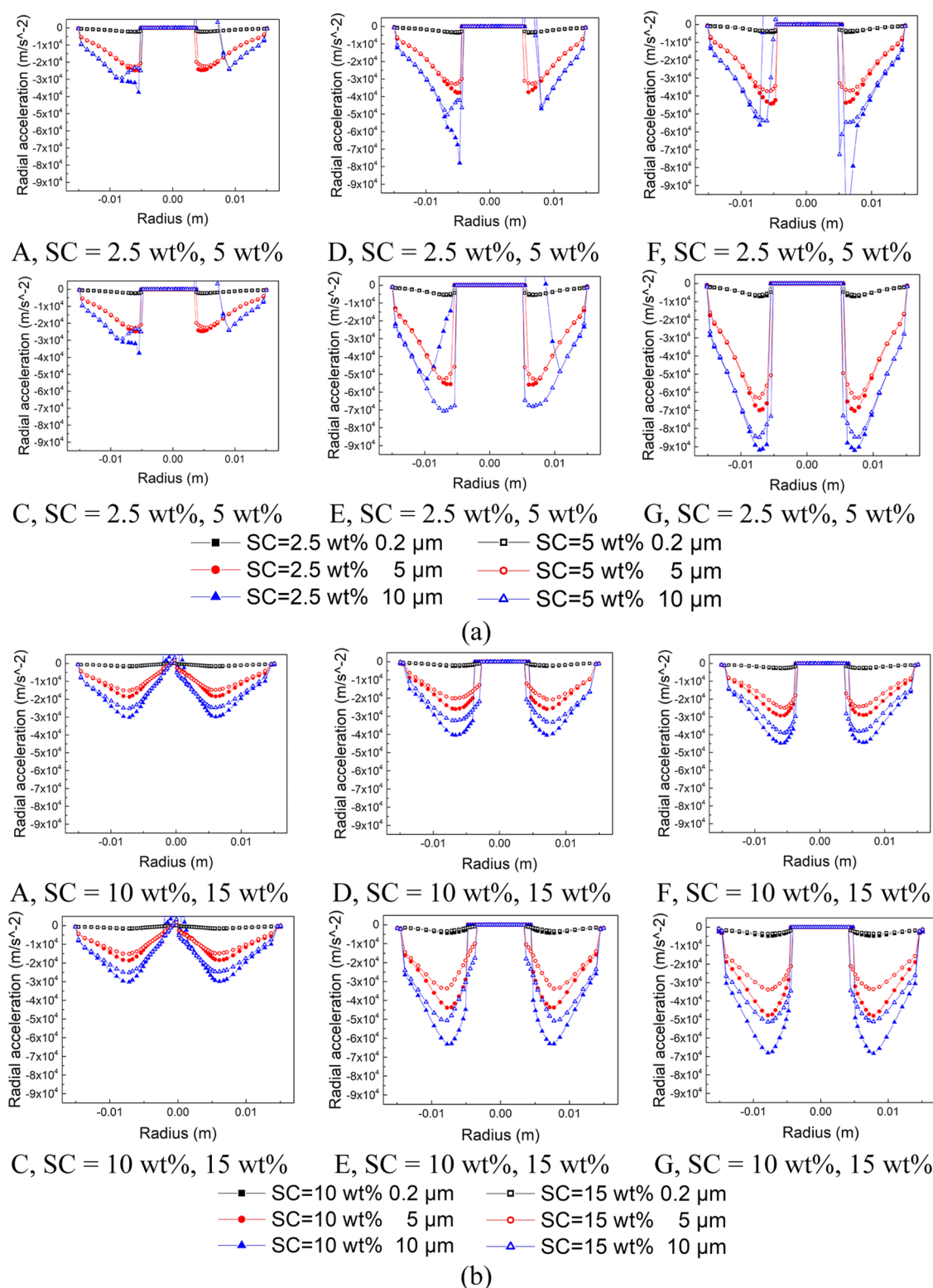
Figure 18. Particle phase radial acceleration (force/mass) distribution in the conical section with SCs of (a) 2.5 or 5 wt % and (b) 10 or 15 wt %: tangential (A, D, and F) and arc (C, E, and G) inlets; cone angles of 10° (A and C), 20° (D and E), and 30° (F and G).

consumption of the kinetic energy and lower motion speed of the particle phase, as indicated by the attenuation of the air core and tangential velocity (Figure 16). As the motion speed of the particle phase decreases, the particles generally have a longer residence time. The change in SC had a smaller effect on the radial acceleration of the fine particles than on that of

the coarse particles (Figure 18). Therefore, increasing SC had a greater impact on the motion of fine particles in terms of residence time. As the residence time increased, more fine particles (<2 μm) were separated to the underflow (Figure 13). However, the dynamic behavior of fine particles (2−5 μm) was also affected to some degree in a manner similar to
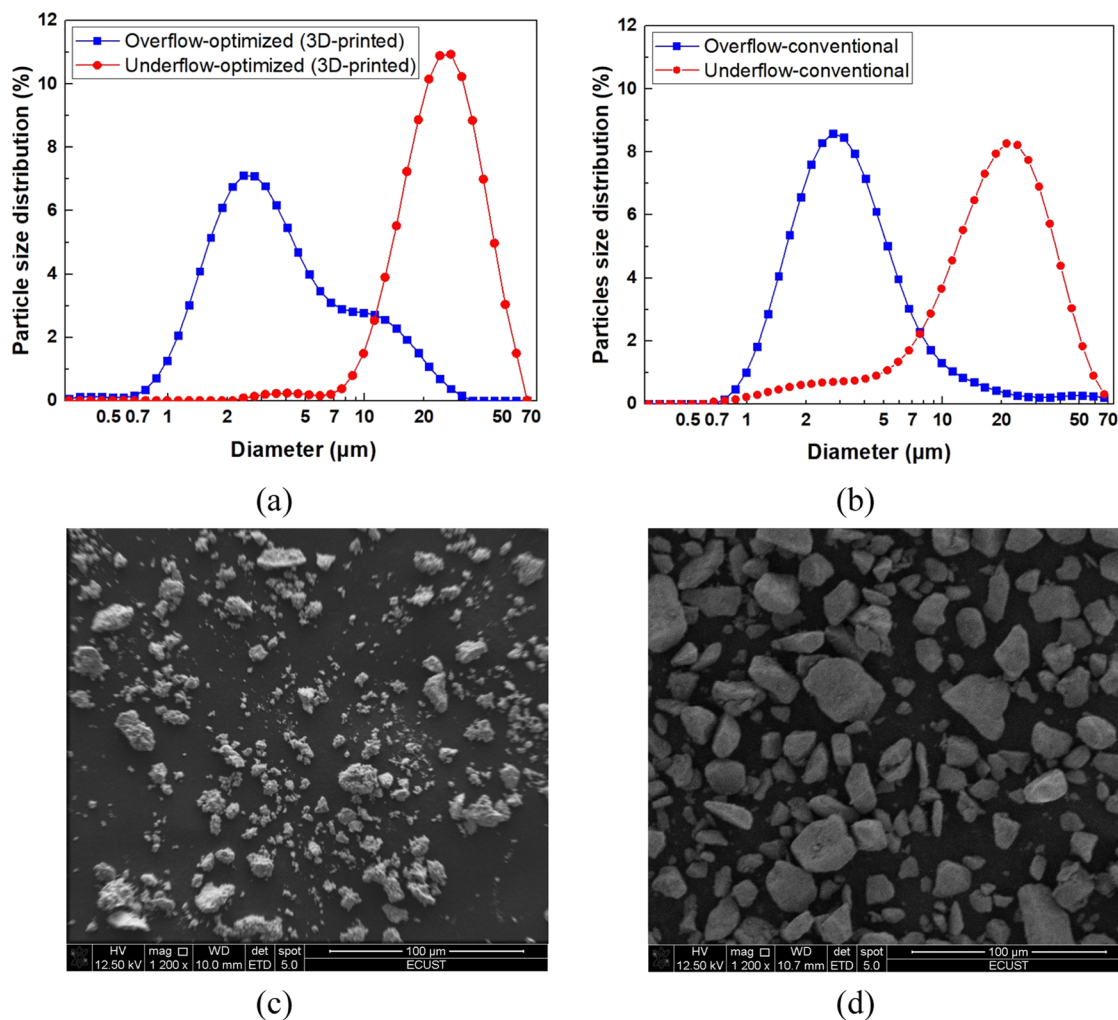
Figure 19. Particle size distribution and SEM images of the experimental products of the hydrocyclones for MnO_2 classification: (a) optimized, (b) conventional, (c) overflow of the optimized hydrocyclone, and (d) underflow of the optimized hydrocyclone.

that of coarse particles. In the case of coarse particles, increasing SC inconsiderably decreased radial acceleration. Thus, the effect of acceleration on coarse particles was greater than that of the residence time. A decrease in radial acceleration led to a decreased separation efficiency of coarse particles, indicating a decline in C_c. In summary, increasing SC increased the residence time and decreased radial acceleration, which had opposite effects on the overflow−underflow partition of the particles. Thus, in contrast to coarse particles, these complex factors explain the nonmonotonic performance of fine particles in Figures 8 and 15.

3.3. Experiments of the Optimized Novel 3D-Printed Hydrocyclone. The particle size distributions for the overflow/underflow of the conventional and optimized novel 3D-printed hydrocyclones are shown in Figure 19a,b. Although the content of the coarse particles (>10 μm) in the overflow of the optimized hydrocyclone was higher than that of the conventional one, the misplacement of fine particles (<5 μm) was significantly eliminated in the underflow of the optimized hydrocyclone. Thus, the particle size of the underflow products was greatly improved. Given that the partition ratio of the particles in the underflow was much higher than that in the overflow, the fine removal effect was satisfactory, whereas the coarse particle loss in the overflow was not affected. SEM images (Figure 19c,d) show the particle size of the products of

the novel 3D-printed hydrocyclone. The size difference between the overflow and underflow products is evident and agrees with the particle size distribution, indicating satisfactory classification.

Table 3 presents the experimental test results of the separation performance indexes. The C_f of the optimized

Table 3. Experimental Classification Performance of Hydrocyclones

	C_f	C_c	S_s	underflow d_{10} (μm)
optimized (3D-printed)	0.930	0.935	0.932	12.4
conventional	0.719	0.946	0.832	5.7

hydrocyclone was significantly better (0.930) than that of the conventional hydrocyclone (0.719). The C_c of the optimized hydrocyclone (0.935) was slightly lower than that of the conventional hydrocyclone (0,946). Further, the average efficiency ($S_s = (C_f + C_c)/2$) of the optimized hydrocyclone was dramatically higher (0.932) than that of the conventional hydrocyclone (0.832). Additionally, the d_{10} of the optimized hydrocyclone was higher. Overall, classification of MnO_2 particles was achieved using the optimized hydrocyclone owing to its combined perclassification and cone section effects discussed in Section 3.2.

4. CONCLUSIONS

Herein, ultrafine particle classification using hydrocyclones has been comprehensively explained using MnO_2 as a case study. The effects of a novel arc inlet and cone angle of the hydrocyclone on ultrafine particle classification under various feed SCs were investigated using CFD simulations with Eulerian−Eulerian methods. The main conclusions are as follows:

(1) The arc inlet provides a preclassification effect on the particles at the inlet section of the hydrocyclone, which helps improve the classification sharpness of micron and submicron particles. Herein, the hydrocyclone with an arc inlet (C) achieves an Ecart probable of 1.46 μm under the SC of 2.5 wt % with a C_f of 0.68 and C_c of >0.99. Further, dynamic analysis also shows that the arc inlet has a positive effect on the fluid field in the main body of the hydrocyclone.

(2) Larger cone angle design is beneficial to micron and submicron fine particle removal; however, it may result in the reduced recovery of coarse particles. The combined design of a large cone and arc inlet provides the best trade-off of these classification requirements, as the preclassification effect of the arc inlet and the combined effect on the fluid field offset the decrease in C_c to some degree.

(3) The combined design of an arc inlet and large cone angle generally provides better reliability than other structures under high SCs. This improvement in the classification effect can be attributed to the comprehensive optimization of radial acceleration and residence time. The design of the arc inlet with a 30° cone angle is the best option under low SCs, whereas the hydrocyclone with an arc inlet and a 20° cone angle is an appropriate alternative under high SCs. With a 10 wt % feed slurry, the C_f of the optimized 3D-printed hydrocyclone is considerably improved (0.930 vs 0.719) with a slight loss in C_c. Satisfactory classification of ultrafine MnO_2 particles has been obtained.

■ AUTHOR INFORMATION

Corresponding Author

Yanxia Xu − National Engineering Research Centre for Integrated Utilization of Salt Lake Resources, School of Resources and Environmental Engineering, East China University of Science and Technology, Shanghai 200237, China; ⊙ orcid.org/0000-0002-2207-3492; Email: xyx@ecust.edu.cn

Authors

Junxiang Ye − National Engineering Research Centre for Integrated Utilization of Salt Lake Resources, School of Resources and Environmental Engineering, East China University of Science and Technology, Shanghai 200237, China

Xingfu Song − National Engineering Research Centre for Integrated Utilization of Salt Lake Resources, School of Resources and Environmental Engineering, East China University of Science and Technology, Shanghai 200237, China; ⊙ orcid.org/0000-0002-1064-5748

Jianguo Yu − National Engineering Research Centre for Integrated Utilization of Salt Lake Resources, School of Resources and Environmental Engineering, East China

University of Science and Technology, Shanghai 200237, China

Complete contact information is available at:
https://pubs.acs.org/10.1021/acsomega.2c06383

Notes

The authors declare no competing financial interest.

■ ACKNOWLEDGMENTS

■ NOMENCLATURE

u	fluid velocity, m/s
t	time, s
p	pressure, Pa
d	particle diameter, m
g	acceleration due to gravity, $9.81 m/s^2$
a	acceleration, m/s^2
C_D	drag coefficient
Re	Reynolds number
w	vortex finder thickness, mm
D_c	cylindrical body diameter, mm
D_i	inlet size, mm
D_o	vortex finder diameter, mm
D_u	spigot diameter, mm
L_o	vortex finder length, mm
L_c	cylindrical part length, mm
γ	cone angle, °

■ REFERENCES

(1) Xi, W. M.; Geissen, S. U. Separation of titanium dioxide from photocatalytically treated water by cross−flow microfiltration. *Water Res.* **2001**, *35*, 1256−1262.

(2) George, P.; Nguyen, A. V.; Jameson, G. J. Assessment of true flotation and entrainment in the flotation of submicron particles by fine bubbles. *Miner. Eng.* **2004**, *17*, 847−853.

(3) Steinigeweg, D.; Schutz, M.; Salehi, M.; Schlucker, S. Fast and cost−effective purification of gold nanoparticles in the 20−250 nm size range by continuous density gradient centrifugation. *Small* **2011**, *7*, 2443−2448.

(4) Huang, A. N.; Ito, K.; Fukasawa, T.; Yoshida, H.; Kuo, H. P.; Fukui, K. Classification performance analysis of a novel cyclone with a slit on the conical part by CFD simulation. *Sep. Purif. Technol.* **2018**, *190*, 25−32.

(5) Bradley, D.; Danckwerts, P. V.*The Hydrocyclone*; Pergamon Press: London, 1965.

(6) Ni, L.; Tian, J. Y.; Song, T.; Jong, Y. S.; Zhao, J. N. Optimizing Geometric Parameters in Hydrocyclones for Enhanced Separations: A Review and Perspective. *Sep. Purif. Rev.* **2019**, *48*, 30−51.

(7) Balestrin, E.; Decker, R. K.; Noriler, D.; Bastos, J. C. S. C.; Meier, H. F. An alternative for the collection of small particles in cyclones: experimental analysis and CFD modeling. *Sep. Purif. Technol.* **2017**, *184*, 54−65.

(8) Bhardwaj, P.; Bagdi, P.; Sen, A. K. Microfluidic device based on a micro−hydrocyclone for particle−liquid separation. *Lab Chip* **2011**, *11*, 4012−4021.

(9) Yu, J. F.; Fu, J.; Cheng, H.; Cui, Z. W. Recycling of rare earth particle by mini−hydrocyclones. *Waste Manage.* **2017**, *61*, 362−371.

(10) Liow, J.-L.; Oakman, O. A. Performance of mini−axial hydrocyclones. *Miner. Eng.* **2018**, *122*, 67−78.

(11) Wang, B.; Yu, A. B. Computational investigation of the mechanisms of particle separation and "fish−hook" phenomenon in hydrocyclones. *AIChE J.* **2009**, *56*, 1703−1715.

(12) Dueck, J.; Farghaly, M.; Neesse, T. The theoretical partition curve of the hydrocyclone. *Miner. Eng.* **2014**, *62*, 25−30.

(13) Bergström, J.; Vomhoff, H. Experimental hydrocyclone flow field studies. *Sep. Purif. Technol.* **2007**, *53*, 8−20.

(14) Chu, K. W.; Wang, B.; Yu, A. B.; Vince, A. Computational study of the multiphase flow in a dense medium cyclone: effect of particle density. *Chem. Eng. Sci.* **2012**, *73*, 123−139.

(15) Narasimha, M.; Mainza, A.; Holtham, P. N.; Powell, M.; Brennan, M. S. A semi−mechanistic model of hydrocyclones— Developed from industrial data and inputs from CFD. *Int. J. Miner. Process.* **2014**, *133*, 1−12.

(16) Kyriakidis, Y. N.; Silva, D. O.; Barrozo, M. A. S.; Vieira, L. G. M. Effect of variables related to the separation performance of a hydrocyclone with unprecedented geometric relationships. *Powder Technol.* **2018**, *338*, 645−653.

(17) Ji, L.; Kuang, S. B.; Qi, Z.; Wang, Y.; Chen, J.; Yu, A. B. Computational analysis and optimization of hydrocyclone size to mitigate adverse effect of particle density. *Sep. Purif. Technol.* **2017**, *174*, 251−263.

(18) Tian, J.; Ni, L.; Song, T.; Olson, J.; Zhao, J. An overview of operating parameters and conditions in hydrocyclones for enhanced separations. *Sep. Purif. Technol.* **2018**, *206*, 268−285.

(19) Evans, W. K.; Suksangpanomrung, A.; Nowakowski, A. F. The simulation of the flow within a hydrocyclone operating with an air core and with an inserted metal rod. *Chem. Eng. J.* **2008**, *143*, 51−61.

(20) Dueck, J.; Pikushchak, E.; Minkov, L.; Farghaly, M.; Neesse, T. Mechanism of hydrocyclone separation with water injection. *Miner. Eng.* **2010**, *23*, 289−294.

(21) Vakamalla, T. R.; Koruprolu, V. B. R.; Arugonda, R.; Mangadoddy, N. Development of novel hydrocyclone designs for improved fines classification using multiphase CFD model. *Sep. Purif. Technol.* **2017**, *175*, 481−497.

(22) Chu, L. Y.; Chen, W. M.; Lee, X. Z. Effect of structural modification on hydrocyclone performance. *Sep. Purif. Technol.* **2000**, *21*, 71−86.

(23) Salvador, F. F.; Barrozo, M. A. S.; Vieira, L. G. M. Effect of a Cylindrical Permeable Wall on the Performance of Hydrocyclones. *Chem. Eng. Technol.* **2016**, *39*, 1015−1022.

(24) Zhao, L.; Jiang, M.; Xu, B.; Zhu, B. Development of a new type high−efficient inner−cone hydrocyclone. *Chem. Eng. Res. Des.* **2012**, *90*, 2129−2134.

(25) Su, T.; Yifei, Z. Effect of the Axially Inserted Solid Rod on the Flow Field Characteristics and Separation Performance of a Hydrocyclone. *ACS Omega* **2022**, *7*, 24208−24218.

(26) Kraipech, W.; Chen, W.; Dyakowski, T.; Nowakowski, A. The performance of the empirical models on industrial hydrocyclone design. *Int. J. Miner. Process.* **2006**, *80*, 100−115.

(27) Chen, W.; Zydek, N.; Parma, F. Evaluation of hydrocyclone models for practical applications. *Chem. Eng. J.* **2000**, *80*, 295−303.

(28) Ji, L.; Chen, J.; Kuang, S. B.; Qi, Z.; Chu, K. W.; Yu, A. B. Prediction of separation performance of hydrocyclones by a PC− based model. *Sep. Purif. Technol.* **2019**, *211*, 141−150.

(29) Hsu, C. Y.; Wu, R. M. Effect of overflow depth of a hydrocyclone on particle separation. *Drying Technol.* **2010**, *28*, 916− 921.

(30) Ghodrat, M.; Kuang, S. B.; Yu, A. B.; Vince, A.; Barnett, G. D.; Barnett, P. J. Numerical analysis of hydrocyclones with different vortex finder configurations. *Miner. Eng.* **2014**, *63*, 125−138.

(31) Ghodrat, M.; Kuang, S. B.; Yu, A. B.; Vince, A.; Barnett, G. D.; Barnett, P. J. Computational study of the multiphase flow and performance of hydrocyclones: effects of cyclone size and spigot diameter. *Ind. Eng. Chem. Res.* **2013**, *52*, 16019−16031.

(32) Wang, C. C.; Wu, R. M. Experimental and simulation of a novel hydrocyclone−tubular membrane as overflow pipe. *Sep. Purif. Technol.* **2018**, *198*, 60−67.

(33) Yamamoto, T.; Oshikawa, T.; Yoshida, H.; Fukui, K. Improvement of particle separation performance by new type hydro cyclone. *Sep. Purif. Technol.* **2016**, *158*, 223−229.

(34) Lanyue, J.; Peikun, L.; Yuekan, Z.; Xiaoyu, L.; Xinghua, Y.; Huilin, X.; Hui, W. Experimental study of the separation performance of a hydrocyclone with a compound curve cone. *Powd. Tech.* **2022**, *409*, No. 117829.

(35) Tang, B.; Xu, Y. X.; Song, X. F.; Sun, Z.; Yu, J. G. Effect of inlet configuration on hydrocyclone performance. *Trans. Nonferrous Met. Soc. China.* **2017**, *27*, 1645−1655.

(36) Feng, L.; Wenxiu, F.; Peikun, L.; Xinghua, Y.; Yuekan, Z.; Xiaoyu, L.; Yulong, Z.; Lanyue, J.; Hui, W. Investigation of optimal design and separation performance of the hydrocyclone with a vorticose involute−line diversion feeding body. *Powder Technol.* **2022**, *405*, No. 117523.

(37) Hwang, K. J.; Hwang, Y. W.; Yoshida, H. Design of novel hydrocyclone for improving fine particle separation using computational fluid dynamics. *Chem. Eng. Sci.* **2013**, *85*, 62−68.

(38) Shakeel Syed, M.; Rafeie, M.; Henderson, R.; Vandamme, D.; Asadnia, M.; Warkiani, M. E. A 3D−printed mini−hydrocyclone for high throughput particle separation: application to primary harvesting of microalgae. *Lab Chip* **2017**, *17*, 2459−2469.

(39) Fan, Y.; Wang, J.; Bai, Z.; Wang, J.; Wang, H. Experimental investigation of various inlet section angles in mini−hydrocyclones using particle imaging velocimetry. *Sep. Purif. Technol.* **2015**, *149*, 156−164.

(40) Zhang, C.; Wei, D. Z.; Cui, B. Y.; Li, T. S.; Luo, N. Effects of curvature radius on separation behaviors of the hydrocyclone with a tangent−circle inlet. *Powder Technol.* **2017**, *305*, 156−165.

(41) Fu, P. B.; Wang, F.; Yang, X. J.; Ma, L.; Cui, X.; Wang, H. L. Inlet particle−sorting cyclone for the enhancement of PM2.5 separation. *Environ. Sci. Technol.* **2017**, *51*, 1587−1594.

(42) Yang, Q.; Lv, W. J.; Ma, L.; Wang, H. L. CFD study on separation enhancement of mini−hydrocyclone by particulate arrangement. *Sep. Purif. Technol.* **2013**, *102*, 15−25.

(43) Wang, B.; Yu, A. B. Numerical study of particle−fluid flow in hydrocyclones with different body dimensions. *Miner. Eng.* **2006**, *19*, 1022−1033.

(44) Qi, Z.; Kuang, S. B.; Yu, A. B. Numerical investigation of the separation behaviours of fine particles in large dense medium cyclones. *Int. J. Miner. Process.* **2015**, *142*, 35−45.

(45) Yoshida, H.; Hayase, Y.; Fukui, K.; Yamamoto, T. Effect of conical length on separation performance of sub−micron particles by electrical hydro−cyclone. *Powder Technol.* **2012**, *219*, 29−36.

(46) Qian, P.; Ma, J.; Liu, Y.; Yang, X. J.; Zhang, Y. H.; Wang, H. L. Concentration distribution of droplets in a liquid−liquid hydrocyclone and its application. *Chem. Eng. Technol.* **2016**, *39*, 953−959.

(47) Wang, B.; Chu, K. W.; Yu, A. B.; Vince, A.; Barnett, G. D.; Barnett, P. J. Computational study of the multiphase flow and performance of dense medium cyclones: effect of body dimensions. *Miner. Eng.* **2011**, *24*, 19−34.

(48) Yang, Q.; Wang, H. L.; Liu, Y.; Li, Z. M. Solid/liquid separation performance of hydrocyclones with different cone combinations. *Sep. Purif. Technol.* **2010**, *74*, 271−279.

(49) Dong, L. P.; Fan, M. Q.; Yang, H. L. Separation performance of a cyclone column separator with complicated positive and negative cones. *Int. J. Miner. Process.* **2013**, *122*, 43−46.

(50) Ghodrat, M.; Kuang, S. B.; Yu, A. B.; Vince, A.; Barnett, G. D.; Barnett, P. J. Numerical analysis of hydrocyclones with different conical section designs. *Miner. Eng.* **2014**, *62*, 74−84.

(51) Vega-Garcia, D.; Brito-Parada, P. R.; Cilliers, J. J. Optimising small hydrocyclone design using 3D printing and CFD simulations. *Chem. Eng. J.* **2018**, *350*, 653−659.

(52) Hwang, K. J.; Chou, S. P. Designing vortex finder structure for improving the particle separation efficiency of a hydrocyclone. *Sep. Purif. Technol.* **2017**, *172*, 76−84.

(53) Kuang, S. B.; Qi, Z.; Yu, A. B.; Vince, A.; Barnett, G. D.; Barnett, P. J. CFD modeling and analysis of the multiphase flow and performance of dense medium cyclones. *Miner. Eng.* **2014**, *62*, 43−54.

(54) Jiang, L. Y.; Liu, P. K.; Yang, X. H.; Zhang, Y. K.; Wang, H.; Xu, C. C. Numerical analysis of flow field and separation characteristics in hydrocyclones with adjustable apex. *Powder Technol.* **2019**, *356*, 941−956.

(55) Tang, B.; Xu, Y. X.; Song, X. F.; Sun, Z.; Yu, J. G. Numerical study on the relationship between high sharpness and configurations of the vortex finder of a hydrocyclone by central composite design. *Chem. Eng. J.* **2015**, *278*, 504−516.

(56) Ye, J. X.; Xu, Y. X.; Song, X. F.; Yu, J. G. Novel conical section design for ultra−fine particles classification by a hydrocyclone. *Chem. Eng. Res. Des.* **2019**, *144*, 135−149.

(57) Mikko, M.; Veikko, T.; Sirpa, K.*On the Mixture Model for Multiphase Flow*, VTT Publications: Finland, 1996.

(58) Schiller, L.; Nauman, A. Z. A drag coefficient correlation. *Z. Ver. Deutsch. Ing.* **1933**, *77*, 318−320.

(59) Tsuo, Y. P.; Gidaspow, D. Computation of flow patterns in circulating fluidized beds. *AIChE J.* **1990**, *36*, 885−896.

(60) Kuang, S. B.; Chu, K. W.; Yu, A. B.; Vince, A. Numerical study of liquid−gas−solid flow in classifying hydrocyclones: Effect of feed solids concentration. *Miner. Eng.* **2012**, *31*, 17−31.

(61) Aketi, V. A. K.; Vakamalla, T. R.; Narasimha, M.; Sreedhar, G. E.; Shivakumar, R.; Kumar, R. Computational Fluid Dynamic study on the effect of near gravity material on dense medium cyclone treating coal using Discrete Phase Model and Algebraic Slip mixture multiphase model. *J. Comput. Multiphase Flow.* **2017**, *9*, 58−70.

(62) Feng, J. A.; Tang, X. Q.; Wang, W. B.; Ying, R.; Zhang, T. A Combined Method in Parameters Optimization of Hydrocyclone. *Math. Probl. Eng.* **2016**, *2016*, No. 9209362.

(63) Tian, J. Y.; Ni, L.; Song, T.; Zhao, J. N. CFD simulation of hydrocyclone−separation performance influenced by reflux device and different vortex−finder lengths. *Sep. Purif. Technol.* **2020**, *233*, No. 116013.

(64) Ghodrat, M.; Qi, Z.; Kuang, S. B.; Ji, L.; Yu, A. B. Computational investigation of the effect of particle density on the multiphase flows and performance of hydrocyclone. *Miner. Eng.* **2016**, *90*, 55−69.

(65) Chu, K. W.; Chen, J.; Wang, B.; Yu, A. B.; Vince, A.; Barnett, G. D.; Barnett, P. J. Understand solids loading effects in a dense medium cyclone: Effect of particle size by a CFD−DEM method. *Powder Technol.* **2017**, *320*, 594−609.

(66) Vakamalla, T. R.; Mangadoddy, N. Numerical simulation of industrial hydrocyclones performance: Role of turbulence modelling. *Sep. Purif. Technol.* **2017**, *176*, 23−39.

(67) Hsieh, K. T.*Phenomenological model of the hydrocyclone*. Ph.D. Thesis, The University of Utah: Ann Arbor, USA, 1988.

(68) Wang, Z. B.; Chu, L. Y.; Chen, W. M.; Wang, S. G. Experimental investigation of the motion trajectory of solid particles inside the hydrocyclone by a Lagrange method. *Chem. Eng. J.* **2008**, *138*, 1−9.

(69) Neesse, T.; Dueck, J.; Minkov, L. Separation of finest particles in hydrocyclones. *Miner. Eng.* **2004**, *17*, 689−696.